
A NUMERICAL INVESTIGATION OF THE ENERGY
TRANSFER OF A BODY UNDER FLUIDELASTIC
GALLOPING

BY H.G.K.G JAYATUNGA

A THESIS SUBMITTED TO MONASH UNIVERSITY IN FULFILMENT OF THE REQUIREMENTS
FOR THE DEGREE OF

DOCTOR OF PHILOSOPHY

Department of Mechanical Engineering

Monash University

October 2015

DEDICATION

“ To Mrs. Malin Bamunuarachchi; whom without, this work would have never seen the light of day. Thank you madam; for your prayers, blessings, guidance, kind words of encourgaement and above all, believeing in me and giving me strength to get back up, when I myslef have given up hope....”

A LIST OF PUBLICATIONS RELATED TO THIS THESIS

Jayatunga, H.G.K.G, Tan, B.T., Leontini, J.S. 2015 A study on the energy transfer of a square prism under fluid-elastic galloping *Journal of Fluids and Structures* **55**,384-397.

NOMENCLATURE

Symbol	Description
a_1, a_3, a_5, a_7	Coefficients of the polynomial to determine C_y
A	Displacement amplitude
c	Damping constant
D	Characteristic length (side length) of the cross section of the body
El	Subscript denoting integration over a single element
$f = \sqrt{k/m}/2\pi$	Natural frequency of the system
f_g	Frequency of galloping
f_s	Frequency of vortex shedding
F_y	Instantaneous force normal to the flow
F_0	Amplitude of the oscillatory force due to vortex shedding
\mathcal{F}	Fourier transform of velocity
g	Index of the data points inside each element in the ξ -direction
h	Variable indicative of resolution of macro-element mesh
i	Index of the data point being considered during construction of the Lagrange polynomial in the ξ -direction
\mathbf{J}	Jacobian operator for coordinate transformation
j	Data point index in computational space in η -direction
k	Spring constant
m	Mass of the body
m_a	Added mass

Continued on next page \rightarrow

← Continued from previous page

Symbol	Description
n	Timestep count to the current timestep
\mathbf{n}	Unit vector in the normal direction to a boundary
P_d	Power dissipated due to mechanical damping
$P_{in} = \rho U^3 D/2$	Energy flux of the approaching flow
P_m	dimensionless mean power
P_t	Power transferred to the body by the fluid
P_s	surface pressure
P_{trial}	Trial solution for pressure
q	Data point index in computational space in ξ -direction
\mathbf{R}	Residual formed when substituting trial solution into governing equations
s	Data point index in computational space in η -direction
t	Time
U	Freestream velocity
U_i	Induced velocity
V_m	velocity magnitude of the flow
\mathbf{V}	Non-dimensional velocity vector, \mathbf{u}/U
\mathbf{V}_{trial}	Trial solution for velocity
\mathbf{V}^*	Intermediate normalised velocity vector at the end of the advection sub-step
\mathbf{V}^{**}	Intermediate normalised velocity vector at the end of the pressure sub-step
\mathbf{V}_{cyl}	Transverse velocity of the cylinder, \mathbf{v}_{cyl}/U
$\mathbf{V}_{cyl}^{(n+1)\dagger}$	First approximation of \mathbf{V}_{cyl} at the end of the timestep during the elastically-mounted cylinder convection substep
$\mathbf{V}_{cyl}^{(n+1)\ddagger}$	Second approximation of \mathbf{V}_{cyl} at the end of the timestep during the elastically-mounted cylinder convection substep

Continued on next page →

← Continued from previous page

Symbol	Description
$\mathbf{V}_{cyl}^{(n+1)'} $	Approximation of \mathbf{V}_{cyl} at the end of the timestep after relaxation during the elastically-mounted cylinder convection substep
$\mathbf{V}^{(n)}$	Normalised velocity vector at timestep n
$\mathbf{V}^{(n+1)}$	Normalised velocity vector at timestep $n + 1$
$\widehat{\mathbf{V}}^*$	Vector of \mathbf{V}^* at the node points
v	Normalised component of velocity in the y -direction
\mathbf{v}_{cyl}	Instantaneous transverse cylinder velocity
x	Cartesian coordinate in the freestream flow direction, positive downstream
y	Cartesian coordinate transverse to the flow direction and span direction
y_{cyl}	Transverse cylinder displacement
$y_{cyl}^{(n+1)\dagger}$	A first approximation to y_{cyl} at the end of the timestep during the elastically-mounted cylinder convection substep
y, \dot{y}, \ddot{y}	Transverse displacement, velocity and acceleration of the body
$\Delta \mathbf{V}_{cyl}$	Change in \mathbf{V}_{cyl} over one timestep
$\Delta \mathbf{V}_{cyl}^\dagger$	First approximation of change in \mathbf{V}_{cyl} over one timestep during the elastically-mounted cylinder convection substep
$\Delta \tau$	The non-dimensional timestep
ϵ	Under-relaxation parameter used during the elastically-mounted cylinder convection substep
η	Coordinate axis in computational space
ξ	Coordinate axis in computational space
$\mathcal{A} = DL$	Frontal area of the body
λ	Inverse time scale of a galloping dominated flow
$\lambda_{1,2}$	Eigenvalues of linearised equation of motion
ρ	Fluid density

Continued on next page →

← Continued from previous page

Symbol	Description
$\omega_n = 2\pi f$	Natural angular frequency of the system
ω_s	Vortex shedding angular frequency
$c^* = cD/mU$	Non-dimensionalised damping factor
$C_y = F_y/0.5\rho U^2 DL$	Normal (lift) force coefficient
$m^* = m/\rho D^2 L$	Mass ratio
Re	Reynolds number
$U^* = U/fD$	Reduced velocity
$Y = y/D$	Non-dimensional transverse displacement
$\dot{Y} = m^* \dot{y}/a_1 U$	Non-dimensional transverse velocity
$\ddot{Y} = m^{*2} D \ddot{y}/a_1^2 U^2$	Non-dimensional transverse acceleration
$\Gamma_1 = 4\pi^2 m^{*2}/U^{*2} a_1^2$	First dimensionless group arising from linearised, Non-dimensionalised equation of motion
$\Gamma_2 = c^* m^*/a_1$	Second dimensionless group arising from linearised, Non-dimensionalised equation of motion
$\zeta = c/2m\omega_n$	Damping ratio
$\theta = \tan^{-1}(\dot{y}/U)$	Instantaneous angle of incidence (angle of attack)
$\Pi_1 = 4\pi^2 m^{*2}/U^{*2}$	Combined mass-stiffness parameter
$\Pi_2 = c^* m^*$	Combined mass-damping parameter

CONTENTS

1	Preliminary remarks	1
2	A review of the literature	2
2.1	Flow induced vibrations	2
2.2	Fluid-elastic galloping	2
2.2.1	Excitation of galloping	2
2.2.2	Quasi-steady state theory	3
2.2.3	Induced force and the shear layers	8
2.2.4	Frequency response	9
2.2.5	Fluid mechanics governing the galloping response	9
2.2.6	Galloping as a mechanism of energy harvesting	10
2.2.7	Review summery and Objectives	12
3	Methodology and validation	13
3.1	Introduction	13
3.1.1	Parameters used	13
3.2	Quasi-steady model	14
	Solving the quasi-steady state equation	15
3.3	Calculation of average power	15
3.4	Direct numerical simulations (DNS)	16
3.4.1	Governing equations	16
3.4.2	Temporal discretisation:Time-splitting	18
	Integration of the substep equations	19
	The convection substep	19

	The pressure substep	22
	The diffusion substep	22
	Spatial discretisation:Spectral element method	23
	Boundary conditions	27
3.4.3	Convergence and validation studies	28
	Domain size	28
	Convergence	28
I	title	31
4	Governing parameters of fluid-elastic galloping	32
4.1	Introduction	32
4.1.1	Static body results	33
4.2	Formulation of the non-dimensionalised parameters Π_1 and Π_2	34
4.3	Quasi-steady state results	37
4.3.1	Classical VIV parameters vs. Π_1 and Π_2	37
4.3.2	High and low Re data	39
4.3.3	Dependence on mass-stiffness, Π_1	41
4.3.4	Dependence on the mass ratio m^*	44
4.3.5	Comparison with DNS data	44
4.4	Summary of the governing parameters of fluid-elastic galloping	52
5	Frequency response of the system	54
5.1	Introduction	54
5.2	Formulating the linear frequency of the system	55
5.3	Frequency data	56
5.3.1	Comparison of all types of frequencies	56
5.3.2	Linear frequency region	57
5.3.3	Non-linear frequency region	58
5.4	Summary of the frequency response of the system	60

6	Influence of fluid dynamics of the system on the extracted power	61
6.1	Introduction	61
6.2	Influence of the shear layers	62
6.3	Static body results	63
6.4	QSS results	65
6.4.1	Mean power output	65
6.4.2	Surface pressure	66
6.4.3	Velocity profiles at the points of flow separation	66
6.5	Fluid-structure interaction (DNS) results	70
6.5.1	Mean power data	70
6.5.2	Flow-filed data	70
6.5.3	Design considerations for a galloping energy extraction system through control of the fluid dynamics.	73
6.6	Summary of Influence of fluid dynamics of the system on the extracted power	74
7	Conclusions	77

CHAPTER 1

PRELIMINARY REMARKS

Fluid-structure interactions surrounds the whole ecosystem we live in. From the blood flow through our veins to the flight of an A-380 airbus, fluid structure interactions have a significant influence in our lives. On the other hand vibrations are another important phenomenon which governs the whole ecosystem. From the process of our respiratory cycle to the facebook status update we put vibrations influences every aspect of our lives and even life as a whole.

Flow induced vibrations are one of the significant phenomenon occurred as a result of fluid structure interactions.

CHAPTER 2

A REVIEW OF THE LITERATURE

2.1 Flow induced vibrations

2.2 Fluid-elastic galloping

Fluid-elastic galloping is one of the common observable flow-induced vibration on a slender body. This is because this phenomenon is most common in civil structures, such as buildings and iced-transmission lines, the term “aeroelastic galloping” is commonly used as the body is driven by wind. However, this mechanism can occur on a slender body immersed in any fluid Newtonian fluid, provided that the conditions to sustain the galloping mechanism are satisfied. This work is based on a general Newtonian flow, thus the term “fluid-elastic galloping” is used throughout this thesis.

2.2.1 Excitation of galloping

Païdoussis et al. (2010) describes galloping as a “velocity dependent and damping controlled” phenomenon. Therefore, in order for a body to gallop, an initial excitation has to be given to that body. While this excitation is mainly caused by the force created from vortex shedding, other fluid instabilities may contribute to this initial excitation. When a bluff body moves along the transverse direction of the fluid flow, it generates a force along the transverse direction. This force, also known as the induced lift and is a resultant of the fluid flow and the motion of the body. When this body is attached to an flexible

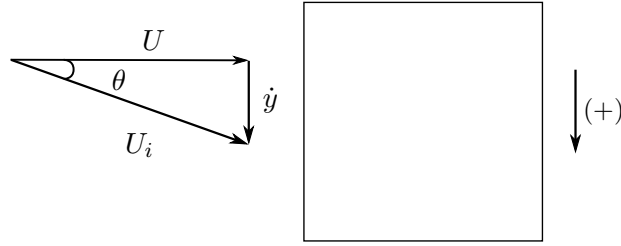


Figure 2.1: Induced angle of attack on the square prism due to the resultant of free-stream velocity of the fluid and transverse velocity of the body.

system (i.e. a system that can be modeled by a spring, mass and damper), the induced lift becomes the periodic forcing of the system. Galloping is sustained if the induced lift is in phase with the motion of the body. This could be explained further by using a square cross section as an example.

Figure 2.1 illustrates the motion of the body at a given instantaneous time. The induced angle of attack is formed on the square cross section as a result of the free stream velocity vector U and the transverse velocity vector of the body \dot{y} . Thus, a force is formed in phase with the motion of the body for the case of a square cross section. This mechanism could also be observed on other bodies which are prone to galloping. The sign convention in this figure (and generally used in this scope of research) states that downward direction is positive. Hence, the force generated on a body under the influence of galloping, could be also identified as a “negative lift”.

2.2.2 Quasi-steady state theory

According Païdoussis et al. (2010), the initial studies by Glauert (1919) provided a criterion for galloping by considering the auto-rotation of a stalled aerofoil. As this phenomenon commonly occur in iced transmission lines, Den Hartog (1956) has provided a theoretical explanation for iced electric transmission lines.

The pioneering study that mathematically models galloping was conducted by Parkinson and Smith (1964). This model has been widely used in almost all subsequent studies on galloping. A weakly non-linear oscillator model was developed by in that study to predict the response of the system. Essentially the quasi-steady assumption was made to develop this model. This assumes that the instantaneous induced lift force of the oscillating body

2. A REVIEW OF THE LITERATURE

is equal to that of the lift force generated by the same body at the same induced angle of attack. For the quasi-steady assumption to be valid, the conditions below have to be satisfied.

- The velocity of the body does not change rapidly
- There is no interaction between vortex shedding and galloping

The second condition is satisfied by ensuring the vortex shedding frequency is much higher than the galloping frequency. The oscillator equation was solved using the Krylov and Bogoliubov method (Parkinson and Smith, 1964). Details of this method is not included in this thesis because this study uses numerical intergration instead. The results obtained form experiments, carried out at $Re = 2200$ and a mass ratio (m^*) around 1164 had a good agreement with the theoretical data which is shown in figure 2.2.

Quasi-steady state oscillator model

The equation of motion of transversely oscillating body is given by

$$m\ddot{y} + c\dot{y} + ky = F_y, \quad (2.1)$$

where the forcing term F_y is given by

$$F_y = \frac{1}{2}\rho U^2 \mathcal{A} C_y. \quad (2.2)$$

As explained previously, the quasi-steady assumption uses the stationary C_y data (which consists of both lift and drag components) for varying angles of attack as inputs to the oscillator equation. Parkinson and Smith (1964) used a 7th order odd interpolating polynomial to interpolate the C_y data. The order of the polynomial can be chosen arbitrarily depending on the study. For example Barrero-Gil et al. (2009, 2010) have used a 3rd order polynomial in order to simplify the analytical model. However, Ng et al. (2005) pointed out that a 7th order polynomial is sufficient as higher order polynomials do not provide significantly better result.

$$C_y(\theta) = a_1 \left(\frac{\dot{y}}{U} \right) - a_3 \left(\frac{\dot{y}}{U} \right)^3 + a_5 \left(\frac{\dot{y}}{U} \right)^5 - a_7 \left(\frac{\dot{y}}{U} \right)^7. \quad (2.3)$$

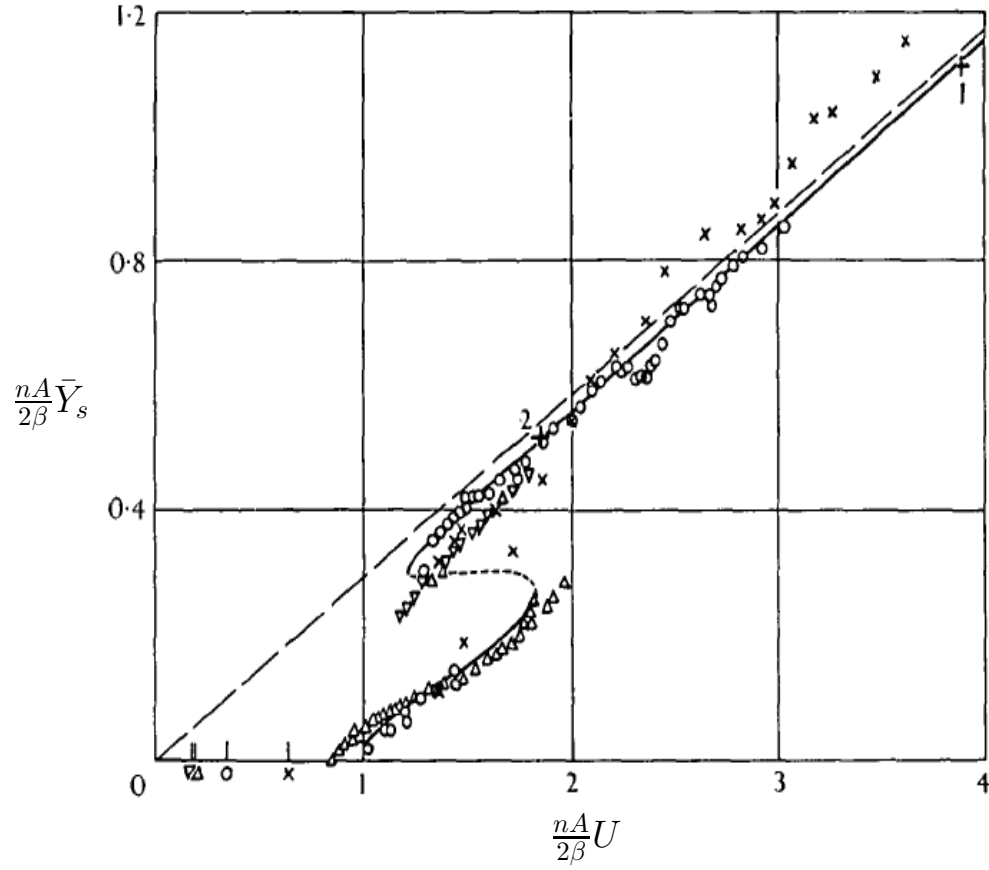


Figure 2.2: “Collapsed amplitude-velocity characteristic. Theory: — stable limit cycle, --- unstable limit cycle. Experiment $\times \beta = .00107$, $\circ \beta = .00196$, $\triangle \beta = .00364$, $\nabla \beta = .00372$, $+ \beta = .0012$, $+ \beta = .0032$ Reynolds numbers 4,000 – 20,000”. Figure extracted from Parkinson and Smith (1964). $\frac{nA}{2\beta} \bar{Y}_s$ is the dimensionless displacement amplitude parameter and $\frac{nA}{2\beta} U$ is the reduced velocity.

2. A REVIEW OF THE LITERATURE

Therefore by substituting the forcing function to the oscillator equation (Eq:2.1) the Quasi-steady state (QSS) model could be obtained (Eq:2.4).

$$m\ddot{y}+c\dot{y}+ky=\frac{1}{2}\rho U^2\mathcal{A}\left(a_1\left(\frac{\dot{y}}{U}\right)-a_3\left(\frac{\dot{y}}{U}\right)^3+a_5\left(\frac{\dot{y}}{U}\right)^5-a_7\left(\frac{\dot{y}}{U}\right)^7\right). \quad (2.4)$$

As the current study is focused on the low Re region, it is a known fact that the vortex shedding will be correlated well and therefore provide a significant forcing. Joly et al. (2012) introduced an additional sinusoidal forcing function to the model in order to integrate the forcing by vortex shedding. By the addition of this forcing Joly et al. (2012) managed to obtain accurate predictions of the displacement amplitude even at low mass ratios, where the galloping is significantly suppressed by the vortex shedding to the point that it is no longer detectable. However, the strength or the amplitude of this sinusoidal forcing has to be tuned in an *ad hoc* manner, and it was not clear the relationship between this forcing with the other system parameters. Thus in the current study this forcing was not used.

Presence of hysteresis

Hysteresis could be observed in the amplitude data of Parkinson and Smith (1964). In contrast, the studies carried out by Barrero-Gil et al. (2009) and Joly et al. (2012) at much lower Reynolds numbers ($159 \leq Re \leq 200$), did not show any hysteresis. Luo et al. (2003) concluded that the hysteresis was present due to the presence of an inflection point in the C_y curve at high Reynolds numbers (Parkinson and Smith (1964) data) which was not present at lower Reynolds numbers. It was further explained and demonstrated by Luo that the inflection point occurs due to the intermittent re attachment of the shear layer in certain angles at high Reynolds numbers.

Figure 2.2.2 shows the vorticity contours of a square cross section obtained at various points of the vortex shedding cycle, at $Re = 1000$, $\theta = 2^\circ$ obtained from Luo et al. (2003). The points 7 and 11 show the intermittent shear layer reattachment which causes the hysteresis in the C_y vs. θ curve at high Reynolds numbers.

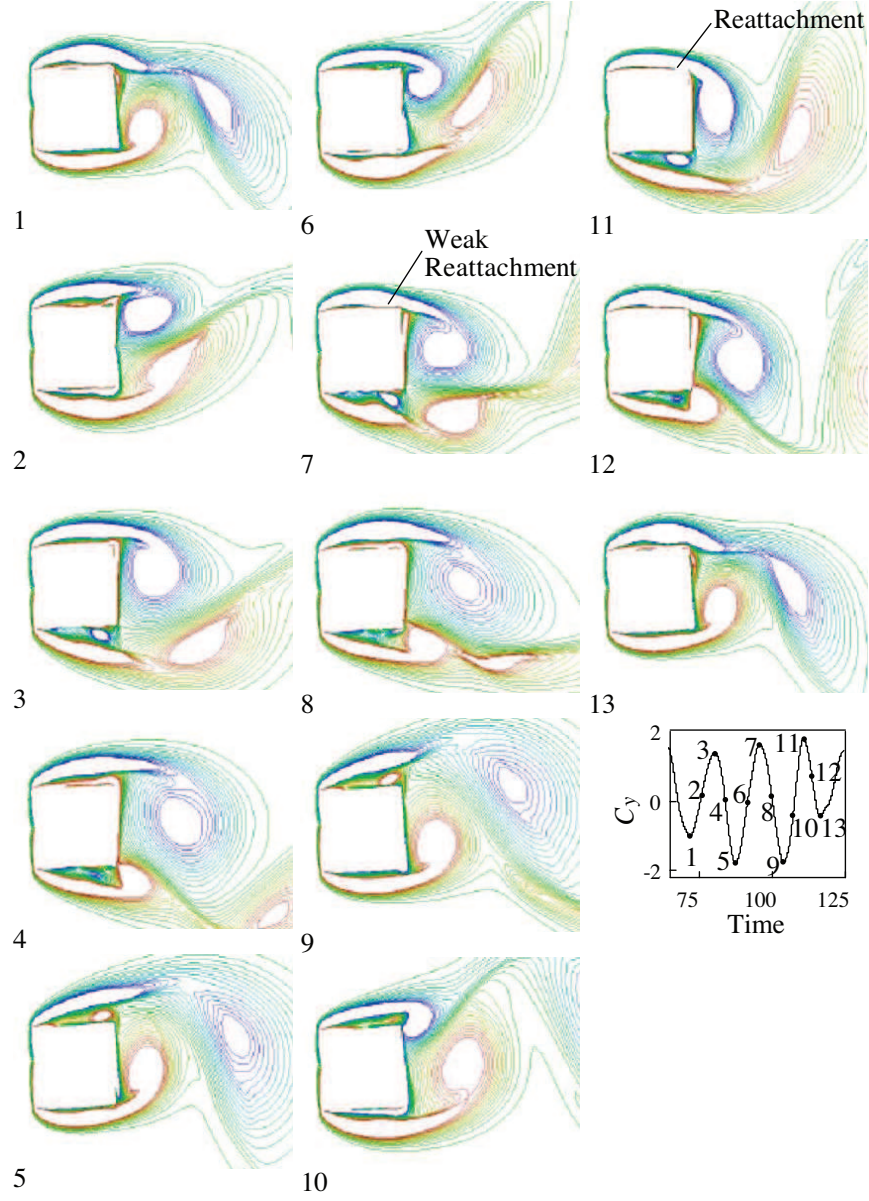


Figure 2.3: Vorticity contours of C_y and the corresponding time for $Re = 1000$, $\theta = 2^\circ$ extracted from Luo et al. (2003). The intermittent shear level is visible in points 7 and 11

2. A REVIEW OF THE LITERATURE

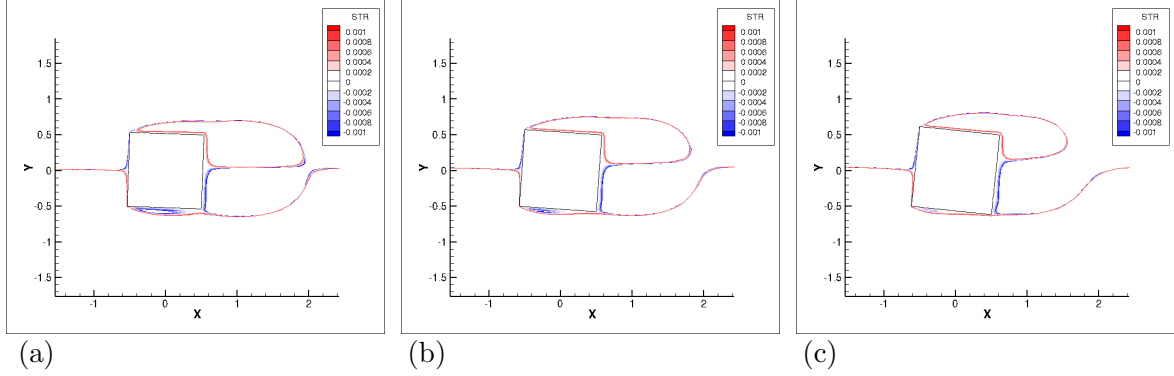


Figure 2.4: Stream functions of time averaged flow field on a stationary square section at $Re = 200$ at different incidence angles. (a) 2° (C_y increases), (b) 4° (C_y peaks) and (c) 2° (C_y decreases). The bottom shear layer comes closer to the bottom wall and reattaches as the angle of incidence increase.

2.2.3 Induced force and the shear layers

It is important to have an understanding on how the induced lift is generated from a fluid dynamics perspective. The quasi-steady model has already been validated and re-validated by many studies (Parkinson and Smith, 1964; Barrero-Gil et al., 2009; Luo et al., 2003), therefore the flow-field data of static body simulations could be used to analyse the underpinning fluid dynamic mechanisms governing galloping.

Gallopings is governed by the the shear layers created at the leading edge due to flow separation on the top and bottom corners of the bluff body. A common example is a square cross section as show in figure 2.4 which has been used widely in studies on galloping. Figure 2.4 shows the stream functions of time averaged (over a vortex shedding cycle) flow fields of stationary cross sections. The angle of incidence (θ) increases clockwise from $2^\circ - 6^\circ$. As θ is increased, the bottom shear layer comes closer to the wall of the body compared to the top shear layer (Figure 2.4 (a)). The shear layer nearer to the body crates higher suction compared to the shear layer at the opposite side. This pressure imbalance between the top and bottom sides of the body creates a downward force (i.e. the negative lift). As the angle is increased, the bottom shear layer becomes closer and therefore the pressure difference becomes grater leading to a higher C_y . The negative lift force becomes maximum when the shear layer near to the wall reattaches at the trailing edge (figure 2.4 (b)). As

θ is further increased, the bubble in the bottom shear layer shrinks in size resulting the reduction of the pressure imbalance of the top and bottom surface leading to the reduction in C_y . This variation of C_y vs θ is presented in figure 4.1. As the body is connected to an oscillatory system (discussed in section 2.2.1), this shear layer behaviour also harmonize with the cyclic behaviour of the system providing the driving force to the system so that the motion of galloping is sustained.

2.2.4 Frequency response

It is clear that the cyclic motion of the shear layer harmonize with the mechanical system. Therefore, the frequency response should be then, the natural frequency of the system ω_n (Païdoussis et al., 2010). This is significantly different from the VIV mechanism, where the primary frequency comes from the periodic forcing of the vortex shedding. Hence, in the QSS model the natural frequency of the system could be identified as the frequency of oscillations. However, it should be noted that this is valid on the regimes where the conditions discussed in section 2.2.2 are satisfied.

The experimental studies carried by Bouclin (1977) concluded at high reduced velocities with large inertia, the motion of the cylinder controls the frequency of the system rather than the vortex shedding. The structural damping has no effect provided that it is small. He also concluded that as the inertia and the reduced velocity gets lower, there is some interaction between vortex shedding and galloping. And at this region the frequency is mainly governed by the vortex shedding.

2.2.5 Fluid mechanics governing the galloping response

As discussed in subsection 2.2.3 the driving force of a galloping system is the asymmetrical placement of the shear layers at either sides of the body. In consequence, it is clear that a significant afterbody is needed for the shear layer interaction to sustain galloping. Parkinson (1974, 1989) and Bearman et al. (1987) have discussed well the importance of the length and the shape for galloping in their reviews. It is also highlighted in Parkinson (1974) that the most important physical parameters for galloping are the size relative to the characteristic height and the shape of the afterbody. Manipulating the shape of the afterbody and thereby, manipulating the shear layer interactions with the body, gives the ability to control the

2. A REVIEW OF THE LITERATURE

galloping response. Thus, due to this reason work has been carried out on the response of galloping of different cross sectional shapes.

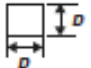
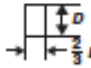
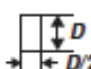

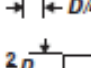
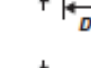
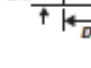
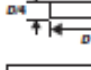
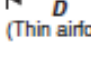



Blevins (1990) provided a good comparison of the shapes which are prone to galloping based on the work by Parkinson and Brooks (1961), Nakamura and Mizota (1975) and Nakamura and Tomonari (1977). The reproduction of Blevins's data could be found in Païdoussis et al. (2010) presented in figure 2.5.

Naudascher and Wang (1993), Ruscheweyh et al. (1996), Deniz (1997) and Weaver and Veljkovic (2005) are some of the work done on different cross sectional shapes. Alonso et al. (2009) carried out wind tunnel tests on biconvex and rhomboidal cross sections. This study concluded that the galloping stability is dependent on the angle of attack. The aspect ratios where these cross sections were isolated. Studies were further carried out by Alonso for elliptical cross sections (Alonso et al., 2010) which concluded that galloping is Reynolds number dependent for elliptical cross sections. The study triangular cross sections carried out by (Alonso et al., 2005) isolated the angle of attacks where galloping is stained. The regions of stability for galloping at different angles of attack and the static force coefficients are presented in these studies with regards to the cross section involved. (Luo et al., 1994) carried out an interesting study where the influence of the afterbody on galloping was investigated. The sides of a square section was chamfered gradually and two trapezoidal cross sections and one isosceles triangle was obtained. The C_y vs. θ plots revealed that the maximum value of C_y increased as the chamfering angle increased (i.e when the cross section was transformed from a square to a isosceles triangle). Another interesting observation is that the angle which this maximum C_y increased as the chamfering angle increased.

2.2.6 Galloping as a mechanism of energy harvesting

The focus on fluid-elastic galloping in the past was on understanding and developing methods to suppress it, due to the adverse effects on civil structures. However, recently, the focus of research has been redirected to develop mechanisms to excite galloping rather than suppressing it. This is due to the recent demand for alternate energy sources with minimal environmental impact. Thus, this demand for alternate energy have lead researchers to develop ways of extracting useful energy from flow induced vibrations.

Bernitsas and his group in the University of Michigan have made significant progress on

Section	h/d	$\partial C_{Fy}/\partial \alpha$		Reynolds number
		Smooth flow	Turbulent flow ^b	
	1	3.0	3.5	10^5
	3/2	0.	-0.7	10^5
	2	-0.5	0.2	10^5
	4	-0.15	0.	10^5
	2/3	1.3	1.2	6.6×10^4
	1/2	2.8	-2.0	3.3×10^4
	1/4	-10.	-	$2 \times 10^3 - 2 \times 10^4$
 (Thin airfoil)	- ^c	-6.3	-6.3	$> 10^3$
	-	-6.3	-6.3	$> 10^3$
	-	-0.1	0.	6.6×10^4
	-	-0.5	2.9	5.1×10^4
	-	0.66	-	7.5×10^4

^a α is in radians; flow is left to right. $\partial C_{Fy}/\partial \alpha = -\partial C_{Ll}/\partial \alpha - C_D$, with C_{Fy} based on the dimension D , so that $\partial C_{Fy}/\partial \alpha > 0$ for galloping.

^b Approximately 10% turbulence.

^c Inappropriate to use h/d .

Figure 2.5: “The transverse force coefficient for various sections in steady smooth or turbulent flow (after Blevins (1990))” obtained from Païdoussis et al. (2010)

2. A REVIEW OF THE LITERATURE

using VIV as potential candidate for energy extraction. Bernitsas et al. (2008) introduced the concept of using VIV as a mode of energy extraction. The group have developed a device called VIVACE converter based on this concept. The work has been further expanded to focus on various aspects (such as Reynolds number effects, damping effects etc.) in Bernitsas et al. (2009); Raghavan et al. (2009); Raghavan and Bernitsas (2011); Lee et al. (2011). This group have studied extensively on the effect of the mechanical parameters, the Reynolds number effects and the bottom boundary conditions of the VIVACE converter, in order to obtain efficient energy output using VIV as an energy harvesting mechanism.

In contrast, the research carried out investigating the possibility of energy harvesting using fluid-elastic galloping is quite limited. Barrero-Gil et al. (2010) conducted the pioneering study on energy harvesting using fluid-elastic galloping. The key consideration to investigate on galloping in this study was that unlike VIV fluid-elastic galloping was not dependent on a synchronisation or a “lock-in” mechanism. Therefore, it could operate on a wide spectrum of frequencies giving fluid-elastic galloping an advantage over VIV as a mechanism of energy harvesting. Vicente-Ludlam et al. (2014) showed that there is a link between the optimal electrical load resistance and the flow speed. However, it was identified that the understanding is a primary and therefore step-by-step research has to be conducted in order to properly understand the link between energy transfer in the galloping mechanism.

2.2.7 Review summery and Objectives

It is clear that more investigations should be carried out on energy transfer of a galloping system, particularly to develop efficient energy harvesting system. More fundamental research is needed to explore the underpinning effects of mechanical and fluid dynamic parameters influencing the energy transfer of a galloping system to fill the gaps of the existing knowledge base. Thus, objectives of the current research were formulated in order to address these research gaps.

CHAPTER 3

METHODOLOGY AND VALIDATION

3.1 Introduction

An overview of the modeling and the computational methods used in this study are presented in this chapter. This study uses well established techniques to model and study fluid elastic galloping. Therefore, only a brief overview is provided together with relevant references where the development and vigorous validation has been presented.

This chapter is presented as follows. The equations used to model the system are presented and discussed. Next, a brief discussion of the techniques used for direct numerical simulations are presented followed by the problem formulation and the discussion of the parameters used. Finally, validation data are presented and discussed to demonstrate the accuracy of the direct numerical simulations.

3.1.1 Parameters used

The findings in this study are presented in two categories i.e. high and low Reynolds numbers, so as to study the system at laminar and turbulent flow regime. One of the main objectives in this study was to capture the flow physics accurately using direct numerical simulations. Hence, major portion of the study was carried out in the laminar range where the flow is laminar and two directional. Although a majority of the study is focused on low Reynolds number regime, some results were presented using inputs from published data at high Reynolds numbers to dare the QSS model and provide a comparison between high

and low Reynolds number cases. $Re = 200$ was defined as the “low” Reynolds number and $Re = 22300$ was defined as the high Reynolds number in this study. Studies by Tong et al. (2008) and Sheard et al. (2009) reveals that the approximate value of 3-dimensional transition of the wake for a square cross section is $Re = 160$ and therefore, $Re = 200$ was selected to represent the low Reynolds number regime, also considering the fact that other numerical studies in the laminar regime have used this value of Reynolds number (Robertson et al., 2003; Joly et al., 2012). All of these published data have used a square cross section as the body of oscillation. Since the basic cross section used in this study is a square, the same flow regimes of the these published data were used.

In the high Reynolds number case, the chosen Reynolds number matches the pioneering study of galloping Parkinson and Smith (1964), from which the stationary aerodynamic data was obtained as input to the QSS model. For the high Re tests, predictions of power output at $Re = 22300$ were obtained using the coefficients of the C_y vs. θ curve from Parkinson and Smith (1964) as inputs to the QSS model. Aerodynamic data (i.e. C_y data) from direct numerical simulations at low Reynold number of stationary cases at different angle of attack are used as inputs to the QSS model at the low Reynolds number regime.

Stationary C_y data at different angles of attack is used as inputs to the QSS model, were obtained for the low Reynolds number regime using direct numerical simulations. The average power was obtained by using equation ??, and the averaging was done over no less than 20 galloping periods. The mass ratio m^* was kept at 1163 for $Re = 22300$ (Similar to Parkinson and Smith (1964)). The parameters used at the low Reynolds number cases are $m^* = 20$ for $Re=200$ and $U^* \geq 40$. These were similar to the parameters used in previous studies (Robertson et al., 2003; Joly et al., 2012). These parameters were used throughout this study unless otherwise specified.

3.2 Quasi-steady model

The quasi-steady state model discussed in section 2.2.2 was used to obtain oscillator response data. The quasi-steady state model has proven its ability to obtain accurate galloping response data (as also discussed in section 2.2.2). Therefore, a large number of cases can be modelled in small amount of computational time. The oscillator equation consist

of spring, mass and damper oscillator expression with a 7th order interpolation polynomial as the forcing function (equation 2.4), obtained from a curve fit of aerodynamic data (i.e. C_y as a function of the incidence angle).

Solving the quasi-steady state equation

The quasi-steady model being an ordinary differential equation could be solved using different solving methods. Some of the techniques include limit cycle oscillations, harmonic balance, cell mapping and numerical integration. Vio et al. (2007) showed that numerical integration provides accurate data. A fourth-order Runge-Kutta ODE solving scheme was used in solving the quasi-steady state oscillator equation. The built in ‘ode45’ function in MATLAB was used primarily to solve the QSS equation while in some cases ‘ode15s’ function was used when the equation became more stiff.

3.3 Calculation of average power

The ideal potential amount of harvested power output could be represented as the dissipated power due to mechanical damping before losses in any power take-off system are included. Thus the mean power output could be expressed as

$$P_m = \frac{1}{T} \int_0^T (c\dot{y})\dot{y}dt, \quad (3.1)$$

where T is the period of integration and c is the mechanical damping constant.

The work done on the body by the fluid is equal to this quantity, defined as

$$P_m = \frac{1}{T} \int_0^T F_y \dot{y}dt, \quad (3.2)$$

where F_y is the transverse (lift) force.

The two definitions of the mean power provide two vital interpretations of power transfer. Equation ?? shows that the power is proportional to the mechanical damping and the magnitude of the transverse velocity. At first glance one may assume that the power could be increased by increasing damping. In a practical power extraction device, the significant component of damping would be due to the electrical generator and therefore, an increase in damping would be due to the increase of the load or in other words the electrical resistance. Yet this perception of damping is not quite accurate as very high damping would

result in reducing the velocity amplitude which then, would not result in a higher energy output according to equation ???. In consequence, a balance need to be obtained where the damping is high, but not to the extent that it will adversely result by overly suppressing the motion of the body.

On the other hand, equation ?? shows that a higher power is attained during situations where the transverse force F_y and the transverse velocity are in phase. Hence, a simple increase in the magnitude of the force or the velocity is not satisfactory to attain a higher power transfer. A higher power output could be obtained when there is a smaller phase difference between the force and the velocity.

3.4 Direct numerical simulations (DNS)

Direct numerical simulations were employed to obtain the stationary data to be used as inputs to the QSS model and to obtain fluid-structure interaction (FSI) predictions to be compared with the QSS model at low Reynolds numbers. A high-order in-house build spectral element which simulates two-dimensional laminar flows was used to obtain the DNS data.

To obtain DNS results an in-house build code was used. This code essentially solves the Navier-Stokes equations in an accelerated reference frame. A three-step time-splitting scheme also known as a fractional step method was used for temporal discretisation. A predictor-corrector method was used for the FSI data where an elastically mounted body was involved. A description of the spectral element method in general can be found in Karniadakis and Sherwin (2005). This code has been very well validated in a variety of fluid-structure interaction problems similar to that studied in the current study (Leontini et al., 2007; Griffith et al., 2011; Leontini et al., 2011; Leontini and Thompson, 2013). A overview of the algorithm is presented in the following subsections which is described in detail by Leontini (2007).

3.4.1 Governing equations

In this study, the following key assumptions were made to carry out the direct numerical simulations.

To formulate the differential equations to an infinitesimally small fluid section, the fluid was assumed to be a continuum. This assumption is valid for all macro flows as is the case in this study.

Next, to avoid the modelling acoustic wave propagation, it was assumed that the density of the fluid is constant. The fluid is incompressible. This particular assumption is usually valid for Mach numbers (ratio of the speed of sound to the speed of fluid flow) less than 0.3.

Finally, the fluid was assumed to be an Newtonian fluid, which means that the shear stress is directly proportional to the strain rate. The assumptions used are quite standard and further information could be found in White (1999).

The Naiver-Stokes equations are the equations which governs a Newtonian, incompressible fluid.

$$\frac{\partial \mathbf{u}}{\partial t} + (\mathbf{u} \cdot \nabla) \mathbf{u} = -\frac{\nabla p_f}{\rho} + \frac{\mu_v}{\rho} (\nabla^2 \mathbf{u}) , \quad (3.3)$$

and continuity,

$$\nabla \cdot \mathbf{u} = 0 . \quad (3.4)$$

The velocity vector field is represented by \mathbf{u} , time by t , the pressure field by p_f fluid density by ρ and the dynamic by μ_v . In the Naiver-Stokes equation (3.3) the left hand side represents the inertial forces and the right hand side represents the pressure forces. The net mass flux into the fluid element is specified to be zero by the continuity equation.

These equations are generalised by non-dimensionalisation. In the case of bluff body wake flows, the equations are non-dimensionalised by using the characteristic length of the body i.e the frontal projected height D , and the free-stream velocity U .

For cases investigating fluid structure interactions the equations are modified to be solved in an accelerated reference frame. The frame of reference is attached to the cylinder. Therefore, an extra term is added to the Naiver-stokes equations which represents the acceleration of the cylinder. Thus, the equations could be written as,

$$\frac{\partial \mathbf{V}}{\partial \tau} = -\nabla P + \frac{1}{Re} (\nabla^2 \mathbf{V}) - (\mathbf{V} \cdot \nabla) \mathbf{V} + \frac{d\mathbf{V}_{cyl}}{d\tau} , \quad (3.5)$$

$$\nabla \cdot \mathbf{V} = 0 . \quad (3.6)$$

3. METHODOLOGY AND VALIDATION

The non dimensional terms are defined s follows: $\mathbf{V} = \mathbf{u}/U$, $\tau = tU/D$, $P = p_f/(\rho U^2)$, $Re = \rho U D/(\mu_v)$, $\mathbf{V}_{cyl} = \mathbf{v}_{cyl}/U$, and \mathbf{v}_{cyl} being the velocity of the cylinder. $\frac{d\mathbf{V}_{cyl}}{d\tau}$, represents acceleration of the cylinder.

The Naiver-Stokes equations are coupled by with the oscillator differential equation

$$\frac{\ddot{y}_{cyl}}{D} + 2\zeta\sqrt{k^*}\frac{\dot{y}_{cyl}}{D} + k^*\frac{y_{cyl}}{D} = \frac{\pi}{2}\frac{C_L}{m^*}, \quad (3.7)$$

Where ζ is the damping ratio, $k^* = kD^2/mU^2$ and $C_L = F_{lift}/(0.5\rho U^2 D)$. The lift coefficient per unit length of the body is C_L , the transverse displacement of the cylinder is given by y_{cyl} , the characteristic length scale of the body is D , k is the spring constant and the mass per unit length of the body is represented by m . The general form of this linear oscillator equation could be found in books such as Naudascher and Rockwell (1994). The final form of the coefficients were constructed by non-dimensionalising the general linear oscillator equation.

3.4.2 Temporal discretisation:Time-splitting

The problem was discretised in order to solve equations 3.5, 3.6 and 3.7 in both space and time. A three-step time splitting method was used for the temporal discretisation. This scheme also known as the fractional step method, was used to separately integrate the terms in the right hand side of the Naiver-Stokes equation (Karniadakis and Sherwin, 2005). The overall integration of one time-step is split into three substeps. An approximate solution of the Naiver-Stokes equation is gained by this scheme.

The cylinder acceleration is integrated through the whole time step in order to obtain a initial approximation of the intermediate velocity filed. This velocity filed is used as the stating condition. The pressure is integrated using this starting condition. A secondary intermediate velocity filed is obtained as a result of the pressure integration substep. This secondary velocity filed is then used as the starting condition for the integration of the diffusion term which results in the final velocity filed.

The three semi-discretised substep equations are as follows:

$$\mathbf{V}^* - \mathbf{V}^{(n)} - \Delta \mathbf{V}_{cyl} = - \int_{\tau}^{\tau+\Delta\tau} (\mathbf{V} \cdot \nabla) \mathbf{V} d\tau \quad (3.8)$$

$$\mathbf{V}^{**} - \mathbf{V}^* = - \int_{\tau}^{\tau+\Delta\tau} \nabla P d\tau \quad (3.9)$$

$$\mathbf{V}^{(n+1)} - \mathbf{V}^{**} = \frac{1}{Re} \int_{\tau}^{\tau+\Delta\tau} \nabla^2 \mathbf{V} d\tau, \quad (3.10)$$

The current time step is represented by n and the intermediate velocity fields at the end the convection and pressure substeps are \mathbf{V}^* and \mathbf{V}^{**} respectively. The change in the body over a time step is given by $\Delta \mathbf{V}_{cyl} = \int_{\tau}^{\tau+\Delta\tau} \frac{d\mathbf{V}_{cyl}}{d\tau} d\tau$.

The addition of these three substep equations reduces to the integrated form of the Naiver-Stokes equation in equation 3.5.

Integration of the substep equations

The integration methods of the pressure, convection and diffusion substeps are presented in this subsection.

The convection substep

As the system involves free oscillation, a coupling between the oscillation equation (equation 3.7) and the Naiver-Stokes equations had to be employed. As a result, the cylinder dynamics had to be solved at each time-step.

An iterative predictor-corrector scheme was employed to obtain the solution of the coupled equations. The initial step being the “predictor” step was obtaining approximations for all the quantities involved in the integration. A quadratic extrapolation was used to obtain an initial estimate of $\Delta \mathbf{V}_{cyl}$ from three previous time step values of \mathbf{V}_{cyl} . Therefore, a non-dynamical approximation could be obtained.

$$\mathbf{V}_{cyl}^{(n+1)\dagger} = 3\mathbf{V}_{cyl}^{(n)} - 3\mathbf{V}_{cyl}^{(n-1)} + \mathbf{V}_{cyl}^{(n-2)}, \quad (3.11)$$

The dagger (\dagger) indicates that the value is an initial approximation eg. $\mathbf{V}_{cyl}^{(n+1)\dagger}$. Thus, $\Delta \mathbf{V}_{cyl}^{\dagger}$ was obtained by a simple subtraction of the value at the current time step.

The approximated position of the cylinder at the next time step could be obtained by carrying out an integration of the cylinder velocity over the time step. A third-order Adams-Moulton method was used to perform the integration. Therefore, the final equation describing the position of the body is given by,

$$\frac{y_{cyl}^{(n+1)\dagger} - y_{cyl}^{(n)}}{\Delta\tau} = \frac{1}{12}(5\mathbf{V}_{cyl}^{(n+1)\dagger} + 8\mathbf{V}_{cyl}^{(n)} - \mathbf{V}_{cyl}^{(n-1)}) \quad (3.12)$$

The transverse displacement of the cylinder is denoted by y_{cyl} , and the.

An offset is present between the cylinder velocity and cylinder position. The velocity of the cylinder is in advance by half a time-step of the position of the cylinder which is $\mathbf{V}_{cyl}^{(n+1)}$ is half a time step is in advance of $y_{cyl}^{(n+1)}$. However, both the cylinder positions and the velocities are located at the same discrete times.

In order to obtain an approximation for \mathbf{V}^* , a solution was obtained for equation 3.8 using the previous approximated quantities.

By using a third-order Adams-Bashforth scheme and incorporating the approximation of equation 3.11 for $\Delta\mathbf{V}_{cyl}^\dagger$ the first approximation for \mathbf{V}^* was obtained using the equation,

$$\frac{\mathbf{V}^* - \mathbf{V}^{(n)} - \Delta\mathbf{V}_{cyl}^\dagger}{\Delta\tau} = \frac{1}{12}(23\mathbf{N}(\mathbf{V})^{(n)} - 16\mathbf{N}(\mathbf{V})^{(n-1)} + 5\mathbf{N}(\mathbf{V})^{(n-2)}) \quad (3.13)$$

The explicit integration method was only used for the first approximation and for the subsequent iterations semi-implicit method was used for \mathbf{V}^* .

This step was followed by solving the remaining substep equations in order to obtain an approximation for $\mathbf{V}^{(n+1)\dagger}$, and then the “predictor” portion of the predictor-corrector method was completed.

The cylinder velocity approximation \mathbf{V}_{cyl}^\dagger , was updated commencing the “corrector” cycle of the predictor-corrector method. This was carried out using a third-order integration scheme.

$$\frac{\mathbf{V}_{cyl}^{(n+1)\dagger} - \mathbf{V}_{cyl}^{(n)}}{\Delta\tau} = \frac{1}{24}(25\ddot{y}_{cyl}^{(n+1)} - 2\ddot{y}_{cyl}^{(n)} + \ddot{y}_{cyl}^{(n-1)}) \quad (3.14)$$

$\Delta\mathbf{V}_{cyl}^\dagger$ was updated using the recalculated value of $\mathbf{V}_{cyl}^{(n+1)\dagger}$. The velocity was integrated over a time step in order to obtain the position of the cylinder. For the first correction cycle a third order Adams-Moulton method was used which completed the first iteration of the predictor-corrector method.

$$\frac{y_{cyl}^{(n+1)\dagger} - y_{cyl}^{(n)}}{\Delta\tau} = \frac{1}{12}(5\mathbf{V}_{cyl}^{(n+1)\dagger} + 8\mathbf{V}_{cyl}^{(n)} - \mathbf{V}_{cyl}^{(n-1)}) \quad (3.15)$$

Slight modifications were employed to the subsequent iterations in order to improve numerical stability. However, the iterations proceeded in a similar manner. As the approximations for $\Delta \mathbf{V}_{cyl}^\dagger$ and $\mathbf{V}^{(n+1)\dagger}$ were available, further correction steps were carried out using third-order Adams-Moulton scheme .

$$\frac{\mathbf{V}^* - \mathbf{V}^{(n)} - \Delta \mathbf{V}_{cyl}^\dagger}{\Delta \tau} = \frac{1}{12}(5\mathbf{N}(\mathbf{V})^{(n+1)\dagger} + 8\mathbf{N}(\mathbf{V})^{(n)} - \mathbf{N}(\mathbf{V})^{(n-1)}) . \quad (3.16)$$

The two remaining substeps were then solved to obtain a new approximation of $\mathbf{V}^{(n+1)\dagger}$.

The first correction step was carried out by employing 3.14 to obtain a second estimate for the velocity of the cylinder $\mathbf{V}_{cyl}^{(n+1)\ddagger}$. A relaxation equation (equation 3.17) was used for the velocity of the cylinder prior to using equation 3.15 since the equations were quite stiff.

$$\mathbf{V}_{cyl}^{(n+1)'} = \mathbf{V}_{cyl}^{(n+1)\dagger} + \epsilon(\mathbf{V}_{cyl}^{(n+1)\ddagger} - \mathbf{V}_{cyl}^{(n+1)\dagger}) , \quad (3.17)$$

$\mathbf{V}_{cyl}^{(n+1)\ddagger}$ and $\mathbf{V}_{cyl}^{(n+1)\dagger}$ represent the most current and previous approximations respectively. The under relaxation parameter is represented by ϵ which controls the proportion of the correction which is considered in each iteration. The final approximation at the end of the relaxation process is represented by $\mathbf{V}_{cyl}^{(n+1)'}$ and was used in equation 3.15 for completing the correction cycle and hence, the iteration.

A convergence error criteria was specified until which the iteration was continued. The lift force of the cylinder, the velocity of the cylinder and the fluid velocity should all converge to the required convergence criteria. A series of convergence studies were carried out in order to obtain the convergence criteria (Pregalato, 2003). The solution converged typically within 3 – 4 iterations and the iteration count exceeded 10 in very rare cases.

The procedure to obtain the solution for \mathbf{V}^* (velocity field at the end of the convection substep) in a nutshell is as follows. A predictor-corrector method was employed, where the primary predictor cycle was first employed. This was followed by obtaining an approximation for $\Delta \mathbf{V}_{cyl}$ which was calculated using equation 3.11. From this approximation ($\Delta \mathbf{V}_{cyl}$) the position of the cylinder was approximated using equation 3.12.

Next, using an explicit Adams-Bashforth scheme, an approximation was obtained for \mathbf{V}^* by solving the substep equation (equation 3.13). The predictor cycle was completed by solving the remaining substep equations to arrive at the first approximation of $\mathbf{V}^{(n+1)}$.

3. METHODOLOGY AND VALIDATION

Then, the primary corrector step was initiated by calculating the forces of the body from the current approximation of $\mathbf{V}^{(n+1)}$. Using these forces together with the current approximations of the velocity and the displacement of the body and the equation of motion of the body (eq:3.7) an approximation for the acceleration of the cylinder at the end of the timestep was obtained. By integrating this acceleration over the timestep using equation 3.14 the corrected approximation of $\Delta\mathbf{V}_{cyl}$ was obtained. Using equation 3.15 the corrected approximation for $y_{cyl}^{(n+1)}$ was obtained by integrating the velocity over a timestep and using the recent value of $\Delta\mathbf{V}_{cyl}$. The primary corrector step and the primary iteration was completed once this step was completed. All the remaining iterations were carried out in a similar manner by with a under relaxation presented in equation 3.17.

The pressure substep

The pressure equation was solved in two parts in order to find solutions the two unknowns i.e. the pressure filed na d the velocity filed at the end of the timestep.

The integration of the pressure substep was initiated by formulating equation 3.9 in terms of a second-order Adams-Moulton scheme which gives,

$$\frac{\mathbf{V}^{**} - \mathbf{V}^*}{\Delta\tau} = -\frac{1}{2}(\nabla P^{(n+1)} + \nabla P^{(n)}) . \quad (3.18)$$

The equation was further reduced by considering that the *RHS* is equal to $\nabla P^{(n+1/2)}$. The divergence portion of equation 3.18 was taken. Using equation 3.6, continuity was applied to the velocity filed which resulted the pressure filed having a Poisson equation of the form of

$$\nabla^2 P^{(n+\frac{1}{2})} = \frac{1}{\Delta\tau} \nabla \cdot \mathbf{V}^* . \quad (3.19)$$

This equation could be solved at the middle of the timestep for the pressure filed. Therefore, this pressure filed could then be back-substituted to equation 3.18, together with the simplified *RHS*, to solve for the velocity filed \mathbf{V}^{**} , at the end of the substep.

The diffusion substep

A numerical stability of the solution scheme has to be considered for the diffusion substep although the equation for diffusion is linear. Therefore, the Crank-Nicholson scheme or the

second order Adams-Moulton scheme which is a semi-implicit scheme and unconditionally numerically stable is employed. Thus this formulates the final equation (eq 3.10) of the time splitting scheme as,

$$\frac{\mathbf{V}^{(n+1)} - \mathbf{V}^{**}}{\Delta\tau} = \frac{1}{2Re}(\nabla^2\mathbf{V}^{(n+1)} + \nabla^2\mathbf{V}^{(n)}) . \quad (3.20)$$

The integration over the timestep is obtained from the solution of this equation for $\mathbf{V}^{(n+1)}$, thus completing the time splitting scheme.

Spatial discretisation:Spectral element method

The spacial discretisation was done using a nodal based spectral-element method. This method is a member of the finite-element class. The computational domain is separated into a series of macro elements and then a continuous solution is obtained over each element. Mesh refinement can be done in the areas where high gradients are experienced, which is also known as h -refinement. It was necessary that all elements to be quadrilateral. Yet, the elements were not restricted from having curved sides.

The calculation of the residual \mathbf{R} initiate the solution process. All the terms of the governing equations (the Navier-Stokes equation eq 3.5) were moved to the *LHS*. Thus, the resulting expression is,

$$\frac{\partial\mathbf{V}}{\partial\tau} + \nabla P - \frac{1}{Re}(\nabla^2\mathbf{V}) + (\mathbf{V}\cdot\nabla)\mathbf{V} - \frac{d\mathbf{V}_{cyl}}{d\tau} = 0 . \quad (3.21)$$

A trial solution is substituted into equation 3.21. The *RHS* of the equation would be zero if the trial solution is exact solution of the equation. If the trial solution is not the exact solution but an approximation to the exact solution which is the case in general, then the *RHS* will be non-zero and a residual will be formed. This residual could be defined by,

$$\frac{\partial\mathbf{V}_{trial}}{\partial\tau} + \nabla P_{trial} - \frac{1}{Re}(\nabla^2\mathbf{V}_{trial}) + (\mathbf{V}_{trial}\cdot\nabla)\mathbf{V}_{trial} - \frac{d\mathbf{V}_{cyl}}{d\tau} = \mathbf{R} , \quad (3.22)$$

The trial solutions for velocity and pressure fields are \mathbf{V}_{trial} and P_{trial} respectively. The error term which is introduced through the trial function is the residual \mathbf{R} . It is clear from equation 3.22 that the definition of the residual is the governing equation substituted by the trial solution substituted to the true solution.

3. METHODOLOGY AND VALIDATION

In order to effectively distribute the error over the domain, the residual has to be weighted in order to minimise the maximum local error. To perform this task the inner product of the residual with a series of weighing functions were taken. The integral of the product of the weighting function and the residual is the inner product of the residual which is set to zero. The method employed here is also commonly known as weighted residual methods.

Tensor-product Lagrange polynomials were used for both interpolating trial functions and weighting functions in the DNS carried out in this study. The order of the polynomials p could be varied from 2 to 14 in order to further improve grid resolution which is also known as p refinement. This p refinement coupled with h refinement leads to a method called $h-p$ method which is used to improve accuracy (Karniadakis and Sherwin, 2005). The method also could be referred as a Galerkin method as both trial and weighting functions used were from the same family of functions. Fletcher (1984, 1991) provides further details on weighted-residual methods and Galerkin method.

Lagrange polynomials could be defined as,

$$L_i(\xi) = \prod_{\substack{g=1 \\ g \neq i}}^{p+1} \frac{(\xi - \xi_g)}{(\xi_i - \xi_g)} \quad (3.23)$$

The special coordinate is ξ and the indices of the data points are represented by i and g and the number of data points are represented by $p + 1$. One of the properties of Lagrange polynomials is that being equal to unity at the point i and being zero at all the other points other than in places in between points. Thus a continuous polynomial which matches the exact values of the velocity at the node point could be obtained when L_i is multiplied by the velocity at point i and then summing over all points. The tensor-product polynomials in two dimensions $N_{q,s}(\xi, \eta)$ could defined as the product of the Lagrange polynomial in one direction $L_q(\xi)$, with that in the other direction $.L_q(\eta)$

The outline of the procedure to find the solution is as follows. The process is initiated by forming inner product of the residual and the tensor-product Lagrange polynomial weighting function.

This gives the integral

$$\int \int_{\Omega} N_{k,m}(\xi, \eta) \cdot \left[\frac{\partial \mathbf{V}_{trial}}{\partial \tau} + \nabla P_{trial} - \frac{1}{Re} (\nabla^2 \mathbf{V}_{trial}) + (\mathbf{V}_{trial} \cdot \nabla) \mathbf{V}_{trial} - \frac{d\mathbf{V}_{cyl}}{d\tau} \right] dx dy = 0 , \quad (3.24)$$

The computational domain is represented by Ω . $N_{q,s}(\xi, \eta)$ which are the weighting function as defined in the computational space.

From equation 3.24 it is shown that each term in the equation is multiplied by the weighting function. Thus, the integral is split into components and the process could be carried out in the each of the substep equations 3.8, 3.9 and 3.10. For example the discretised equation for 3.13 could be expressed as

$$\begin{aligned} & \frac{1}{\Delta \tau} \int \int_{\Omega} N_{q,s}(\xi, \eta) \cdot (\mathbf{V}_{trial}^* - \mathbf{V}_{trial}^{(n)} - \Delta \mathbf{V}_{cyl}) dx dy = \\ & \int \int_{\Omega} N_{q,s}(\xi, \eta) \cdot \left(\frac{1}{12} (23\mathbf{N}(\mathbf{V}_{trial})^{(n)} - 16\mathbf{N}(\mathbf{V}_{trial})^{(n-1)} + 5\mathbf{N}(\mathbf{V}_{trial})^{(n-2)}) \right) dx dy . \end{aligned} \quad (3.25)$$

This integral could be broken into components. Hence, the first term of the of the LHS of equation 3.25 could be defined as,

$$\int \int_{\Omega} \mathbf{V}_{trial}^* N_{q,s}(\xi, \eta) dx dy . \quad (3.26)$$

The first term in equation 3.13 could be used as an example to illustrate the process of obtaining the solution using the spectral element method. In order to calculate the integral of equation 3.26 over the entire computational domain, the integral is evaluated over each element separately. After that, the contributions of each element are summed together.

All the quadrilateral elements are mapped to a square ranging between $-1, 1$ in both directions where ξ and η are the orthogonal coordinates of this square. The approximation of the integral is simplified by defining the internal node points with the Gauss-Lobatto-Legendre (GLL) quadrature.

A Jacobian is introduced to perform this coordinate transformation and hence, the integral over each element becomes,

$$\int \int_{El} \mathbf{V}^* N_{q,s}(\xi, \eta) \mathbf{J}(\xi, \eta) d\xi d\eta , \quad (3.27)$$

The Jacobian is represented by \mathbf{J} and “ El ” denotes that the integration is performed over a single element. The solution of equation 3.27 \mathbf{V}_{trial}^* , could be re-written as a summation of Lagrange polynomial components. This equation also expresses the tensor-product

3. METHODOLOGY AND VALIDATION

Lagrange polynomials representing the weighting functions in directions of ξ and η . Therefore, the equation could be expressed as,

$$\int \int_{El} \sum_{i,j} \widehat{\mathbf{V}}^* L_i(\xi) L_j(\eta) L_q(\xi) L_s(\eta) \mathbf{J}(\xi, \eta) d\xi d\eta . \quad (3.28)$$

The velocity in the nodal points are represented by $\widehat{\mathbf{V}}^*$, L is the one-dimensional Lagrange polynomial and i and j represents the node index in directions ξ and η .

The Gauss-Lobatto Legendre (GLL) quadrature could be used to obtain an approximation to the integral in equation 3.28, taking the definition of the location of the internal points in the computational domain. Thus approximation of 3.28 could be expressed as,

$$\sum_{a,b} W_{a,b} \sum_{i,j} \widehat{\mathbf{V}}^*_{i,j} L_i(\xi_a) L_j(\eta_b) L_q(\xi_a) L_s(\eta_b) \mathbf{J}(\xi_a, \eta_b) . \quad (3.29)$$

$W_{a,b}$ represents the weighting coefficient for GLL quadrature, a and b represents the position of the node in the direction ξ and η respectively.

Even though equation 3.29 appears to be quite intimidating to deal with, the expression could be considerably simplified because of the fact that the system is discrete and the only the values at the nodal points are considered. Incorporating Lagrange polynomials allows the substitution

$$L_i(\xi_a) = \delta_{ia} = \begin{cases} 1 & i = a \\ 0 & i \neq a \end{cases} . \quad (3.30)$$

The Kronecker delta is expressed by δ_{ia} . This substitution leads to a significant reduction of the non-zero elements in the simulation and leads to a much simpler expression. If the convection substep (example considered here) is considered, only a single term remains based on the \mathbf{V}^* term in the convection substep equation which is,

$$W_{q,s} \mathbf{J}(\xi_q, \eta_s) \widehat{\mathbf{V}}^*_{q,s} . \quad (3.31)$$

All the governing terms could be simplified similarly and this process is repeated over all elements. A global matrix is assembled by collecting the contribution of each element

and then this matrix system is solved to obtain solution for the unknown velocity and pressure fields at the nodal points.

Only the continuity of each function is required across the boundaries, with no condition imposed on the gradient (this condition is known as C_0 continuity), even though the shape functions are higher-order polynomials within each element. It can be shown that the method achieves global exponential convergence (Karniadakis and Sherwin, 2005).

The numerical process used for this study has been demonstrated to give exponential spatial convergence as the number of internal nodes per element is increased (Thompson et al., 1996).

Boundary conditions

The boundary conditions, regardless of the mesh were common for all the simulations performed. A no-slip condition was applied to the cross section wall. This condition ensures that the velocity is zero at the surface of the cross section. For stationary simulations a Dirichlet boundary condition is applied. For FSI cases a time-dependent Dirichlet boundary condition was employed for the velocity on the inlet and lateral boundaries. A Dirichlet boundary condition should have a specified value for the variables (Kreyszig, 2010) in this case velocity. The time-dependent Dirichlet condition has to be implemented for the FSI cases to account for the accelerated reference frame attached to the cross section. Thus, the inlet boundary was set to $u = U$ and $v = -\dot{y}$ for FSI cases and $v = 0$ for stationary cases, where u, v are the velocities in the x and y directions, respectively.

The outlet which is at the boundary downstream of the body was assigned the Neumann boundary condition (where the gradient of a property is specified Tu et al. (2008)), $\frac{\partial \mathbf{V}}{\partial \mathbf{n}} = 0$ where \mathbf{n} denotes the unit normal vector. This assumes that the flow does not spatially while exiting the domain.

A Neumann condition for the pressure was applied at all the boundaries except the outlet. The normal gradient was calculated from the Navier–Stokes equations. A Dirichlet condition for the pressure ($p = 0$) was enforced at the outlet. The details of the method can be found in Thompson et al. (2006, 1996)

Although the physical validity of the outlet boundary condition is not quite true, this does not turn out to be a significant problem provided that the Reynolds numbers are low

and the domain is sufficiently far away from the body.

3.4.3 Convergence and validation studies

Domain size

For all cases, a rectangular domain was employed where the inlet was placed $20D$ from the centre of the body, while the outlet was situated $60D$ away from the centre of the body. The lateral boundaries were placed $20D$ away from the centre of the body. The macro element arrangement of the general domain is shown figure 3.1. The macro element arrangement near the cross section was altered to cater for different cross sections. The near wall macro element configuration for the different cross sections are presented in figure 3.2.

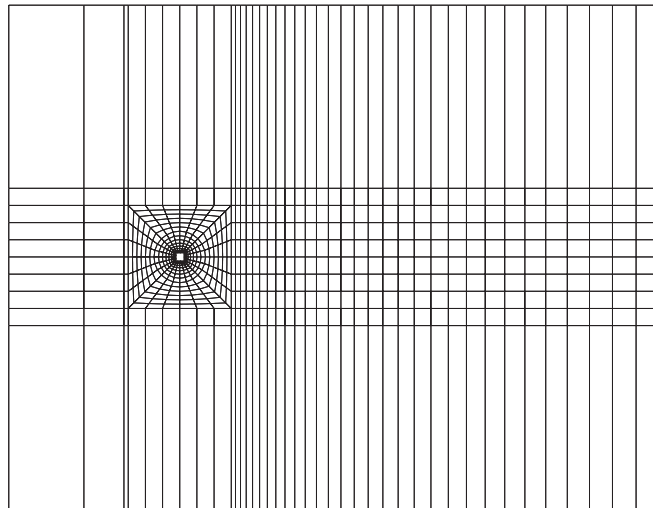


Figure 3.1: Macro element arrangement in the domain for the square cross section geometry. The inlet extending $20D$ upstream from the centre of the body, while the outlet extends $60D$ downstream from the centre of the body. The lateral boundaries were placed $20D$ away from the centre of the body

Convergence

A series of simulations were carried out in order to ensure the results were grid independent. This was done by keeping the layout of the macro element the same and varying the

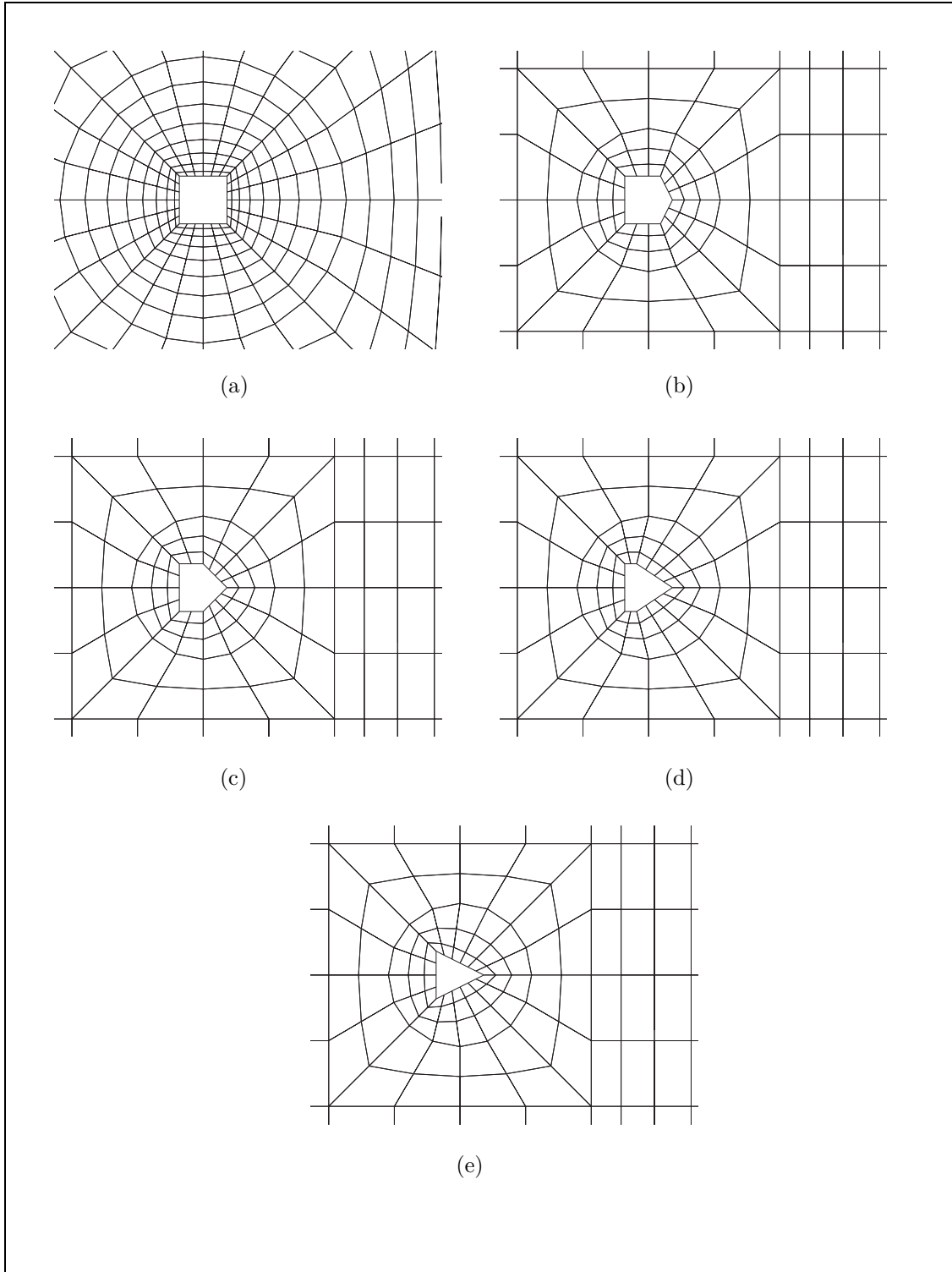


Figure 3.2: Configuration of the macro elements near the cross section. (a) square, (b) $\frac{d}{l} = 0.75$, (c) $\frac{d}{l} = 0.5$, (d) $\frac{d}{l} = 0.25$ and (e) triangle.

3. METHODOLOGY AND VALIDATION

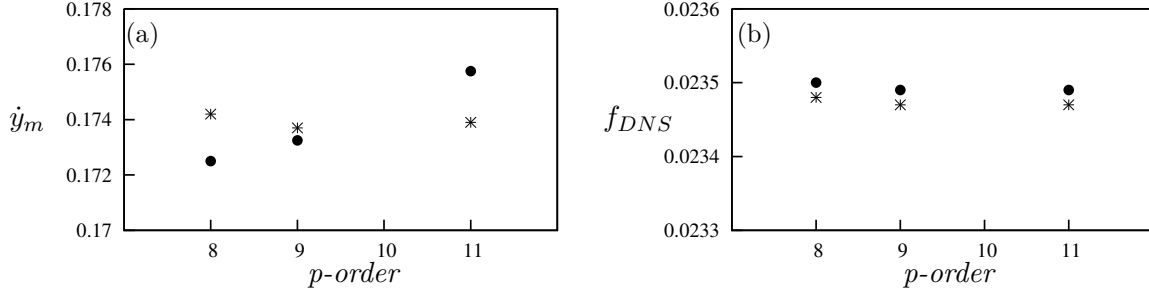


Figure 3.3: Mean velocity amplitude (\dot{y}_m) (a) and the galloping frequency (f_{DNS}) (b) as a function of the interpolation polynomial. Data present $\frac{tU}{D} = 0.001$ (*) and $\frac{tU}{D} = 0.0005$ (•). Data acquired $Re = 200$ $\Pi_2 = 0$ using FSI direct numerical simulations.

order of the interpolation polynomial (p -refinement). The displacement amplitudes were compared against various polynomial orders. The time step is also reduced as the spatial resolution increases to satisfy the Courant condition. The summary of the results are presented in 3.3 .

Figure 3.3 shows the mean velocity amplitude (sub-figure (a)) and the galloping frequency (sub-figure (b)) at different polynomial orders. Two factors namely, the quantitative accuracy of the data and the computational time had to be considered during the decision making process to obtain the optimum spatial and temporal resolution. Even though higher order polynomials gave very accurate data, the time step has to be reduced accordingly to meet the Courant condition and therefore increasing computational time. Thus a 9th order polynomial was incorporated with $\frac{tU}{D} = 0.001$ time-step. A difference of less than 1% could be achieved for both mean velocity amplitude of the body and galloping frequency using this spatial and temporal parameters.

The FSI simulations for other cross sections presented in this thesis were also carried out using these spatial and temporal parameters.

Part I

title

CHAPTER 4

GOVERNING PARAMETERS OF FLUID-ELASTIC GALLOPING

4.1 Introduction

This chapter contains the formulation of non dimensional governing parameters namely, the combined mass-stiffness Π_1 and the combined mass-damping Π_2 and the results and discussion demonstrating the influence of them. These parameters are formulated by obtaining the relevant time-scales of the system followed by non-dimesnionlising the governing QSS oscillator equation.

First, the static body results are presented and discussed. Then, a comparison of Quasi-steady state data presented using the classical VIV parameters and the newly formulated Π_1 and Π_2 is presented and it is concluded that Π_2 provides a better collapse for velocity amplitude and mean power compared the classical reduced velocity (U^*) particularly because unlike U^* , Π_2 does not include a frequency component in it. This is followed by the presentation of QSS data and discussion on the influence of Π_1 and Π_2 on power, which concludes that the power transfer is a primary function of Π_2 and a weak function of Π_1 .

Following this, a comparison of the QSS data with Direct Numerical Simulations (DNS) is presented. This reveals that the power transfer of the DNS data is strongly influenced by both Π_1 and Π_2 . Further analysis reveals that there is a good agreement between QSS and DNS for velocity and power at substantially high Π_1 . As Π_1 decreases, the deviation

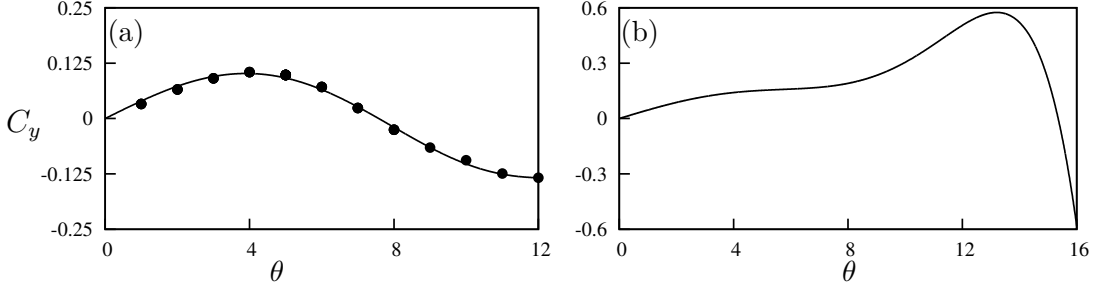


Figure 4.1: Lift coefficient, C_y , as a function of incidence angle θ , for a static square cross section. (a) Data from simulations at $Re = 200$ (b) data from Parkinson and Smith (1964) at $Re = 22300$. Points (\bullet) are measurements from the simulations. At $Re = 200$. Curves in both plots are 7th-order interpolating polynomials used to predict the fluid forcing for the QSS model. C_y is the force coefficient of the force which occurs normal to the induced velocity.

(between QSS simulations and DNS) increases. Power spectral analysis of the DNS data shows a significant response at the vortex shedding at low Π_1 . The relative strength was found out to be an inverse function of Π_1 , which provides a clear explanation for the deviation between QSS simulations and DNS data at low Π_1 . This is primarily due to the influence of vortex shedding where this effect is not accounted in the QSS model.

4.1.1 Static body results

Figure 4.1 shows the plots C_y as a function of θ , as well as the interpolation polynomials. For high Re the polynomial incorporated by Parkinson and Smith (1964) was used. For low Re a 7th order polynomial was fitted using nonlinear least-squares regression. The coefficients of these polynomial fits are shown in table 4.1.

There are several differences that can be observed between high and low Reynolds number data. The peak value of C_y is significantly lower at $Re = 200$ ($C_y = 0.12$ at 5°) compared to $Re = 22300$ ($C_y = 0.57$ at 13°). The inflection point present around 8° for $Re = 22300$ is not present at $Re = 200$. This agrees with the findings of Luo et al. (2003). It was concluded by Luo et al. (2003) that hysteresis in the system response occurs due to the inflection point in the C_y curve. Therefore hysteresis is not expected at $Re = 200$.

The range of incident flow angles where C_y remains positive is narrow at $Re = 200$

Case	a_1	a_3	a_5	a_7
$Re = 200$	2.32	197.8	4301.7	30311.9
$Re = 22300$	2.69	168	1670	59900

Table 4.1: Coefficient values used in the 7th order interpolation polynomial for high ($Re = 22300$) and low ($Re = 200$) Reynolds numbers. These data are used as input data to calculate the right-hand side of Eq. 2.4 throughout this study.

($0^\circ < \theta \leq 7^\circ$) compared to $Re = 22300$ ($0^\circ < \theta \leq 15^\circ$). This feature is what sustains galloping. Power is only transferred from the fluid to the supporting structure within this range of incident angles because fluid forces are acting in the direction of travel of, or in phase with, the oscillating body as demonstrated by equation ???. Incident angles beyond this range actually suppress the galloping and power is transferred in the opposite direction, i.e; from body to fluid. Therefore due to the overall smaller C_y and narrow range of angles where C_y is positive for $Re = 200$ compared to $Re = 22300$, it is expected that the transferred power at $Re = 200$ is significantly lower than at $Re = 22300$.

4.2 Formulation of the non-dimensionalised parameters Π_1 and Π_2

The natural time scales of the system could be obtained by linearising the quasi-steady equation of motion, (Eq:2.4) and finding the eigenvalues. The non-linear terms of the forcing function are truncated and the equation of motion could be expressed as,

$$m\ddot{y} + c\dot{y} + ky = \frac{1}{2}\rho U^2 \mathcal{A}a_1 \left(\frac{\dot{y}}{U} \right), \quad (4.1)$$

After combining the \dot{y} terms and solving for eigenvalues the following solutions for the eigenvalues could be obtained.

$$\lambda_{1,2} = -\frac{1}{2} \frac{c - \frac{1}{2}\rho U \mathcal{A} a_1}{m} \pm \frac{1}{2} \sqrt{\left[\frac{c - \frac{1}{2}\rho U \mathcal{A} a_1}{(m)} \right]^2 - 4 \frac{k}{m}}. \quad (4.2)$$

Galloping essentially occurs at low frequencies therefore it can be assumed that the spring is relevantly weak and therefore, $k \rightarrow 0$. Hence a single non-zero eigenvalue remains which is,

$$\lambda = -\frac{c - \frac{1}{2}\rho U \mathcal{A} a_1}{m}. \quad (4.3)$$

Further, if it is assumed that the mechanical damping is weaker than the fluid dynamic forces on the body the non zero eigenvalue could be further simplified to,

$$\lambda = \frac{\frac{1}{2}\rho U \mathcal{A} a_1}{m}. \quad (4.4)$$

In this representation λ represents the inverse time scale of the motion of the body due to the effect of long-time fluid dynamic forces (or forced due to the induced velocity). This term could also be re-written and λ could be expressed as

$$\lambda = \frac{a_1}{m^*} \frac{U}{D} \quad (4.5)$$

This form clearly shows the significant parameters that influences the inverse time scale of the system. $\partial C_Y / \partial \alpha$, the rate of change in the fluid dynamic force on the body, with respect to the induced angle of attack, is represented by a_1 . $\frac{U}{D}$ represents the inverse advective time scale of the incoming flow, and the mass ratio is resented by m^* . Increasing a_1 would result in a rapid change of the fluid dynamic force with a small change of the induced angle θ , which is proportional to transverse velocity \dot{y} . It can be seen in equation 4.5 that an increase of a_1 would result in an increase of the inverse time scale or decrease the response time of the body. In contrast the mass ratio has the opposite effect where an increase in m^* will lead to a decrease in λ , since a heavier body (or a body with higher inertia) would have a slower response.

In order to find the relevant dimensionless groups of the problem, the time scale formulated could be used to non-dimensionalise the equation of motion. The equation of motion presented in Equation 2.4 can be non-dimensionalised using the non dimensional time τ ,

4. GOVERNING PARAMETERS OF FLUID-ELASTIC GALLOPING

defined as $\tau = t(a_1/m^*)(U/D)$. The non-dimensional equation of motion could then be represented as,

$$\ddot{Y} + \frac{m^{*2}}{a_1^2} \frac{kD^2}{mU^2} Y = \left(\frac{1}{2} - \frac{m^*}{a_1} \frac{cD}{mU} \right) \dot{Y} - \frac{a_1 A_3}{m^{*2}} \dot{Y}^3 + \frac{a_1^3 a_5}{m^{*4}} \dot{Y}^5 - \frac{a_1^5 a_7}{m^{*6}} \dot{Y}^7. \quad (4.6)$$

The equation could be further altered by regrouping the coefficients into non-dimensional groups and could be expressed as,

$$\ddot{Y} + \frac{4\pi^2 m^{*2}}{U^{*2} a_1^2} Y = \left(\frac{1}{2} - \frac{c^* m^*}{a_1} \right) \dot{Y} - \frac{a_1 A_3}{m^{*2}} \dot{Y}^3 + \frac{a_1^3 a_5}{m^{*4}} \dot{Y}^5 - \frac{a_1^5 a_7}{m^{*6}} \dot{Y}^7, \quad (4.7)$$

U^* is the reduced velocity which is the typical independent variable used in vortex-induced vibration studies. c^* is the non-dimensional damping parameter which is expressed as $c^* = cD/mU$.

By analysing equation 4.7 it is clear that five dimensionless parameters play a role in setting the response of the system. These are namely the stiffness, damping, mass ratio, the geometry and the Reynolds number. The stiffness is represented by the reduced velocity U^* , the damping by c^* and the mass ratio by m^* . The geometry and the Reynolds number are represented by the coefficients a_n , of the polynomial fit to the C_y curve. Using the natural time scales of the system, grouping of these non-dimensional parameters into two groups in the non-dimensional equation of motion, suggests that there are two groups that govern the response which are: $\Gamma_1 = 4\pi^2 m^{*2}/U^{*2} a_1^2$ and $\Gamma_2 = c^* m^*/a_1$. Γ_1 could be described as a combined mass-stiffness, where Γ_2 could be expressed as a combined mass-damping parameter for a given geometry and a Reynolds number. It is assumed that the stiffness plays a minor role, Γ_2 seems more likely parameter to collapse the data. The wind tunnel data in the classic paper of galloping by (Parkinson and Smith, 1964) adopted a parameter similar to Γ_2 to collapse the data.

All of the quantities that formulate Γ_1 and Γ_2 except a_1 in theory, could be obtained before an experiment. However in order to obtain the value of a_1 static body experiments are required making it relatively difficult to obtain. Here, the Re and the geometry remains constant and therefore multiplying Γ_1 with a_1^2 and Γ_2 with a_1 suitable parameters could be obtained, and formulate a mass-stiffness parameter $\Pi_1 = 4\pi^2 m^{*2}/U^{*2}$, and a mass-damping parameter defined as $\Pi_2 = c^* m^*$. Therefore equation 4.7 can be written in terms of Π_1 and Π_2 .

$$\ddot{Y} + \Pi_1 Y = \Pi_2 \dot{Y} - \frac{a_1 a_3}{m^{*2}} \dot{Y}^3 + \frac{a_1^3 a_5}{m^{*4}} \dot{Y}^5 - \frac{a_1^5 a_7}{m^{*6}} \dot{Y}^7, \quad (4.8)$$

From equation 4.8, it is clear that the governing parameters of the non dimensionlised equation are Π_1 Π_2 and m^* . However, form closer inspection it is possible to see that m^* has an impact on the non-linear terms of the forcing function. The velocity pf the and hence the induced angle of attack needs to be very high in order for the non-linear terms to be applicable.

4.3 Quasi-steady state results

4.3.1 Classical VIV parameters vs. Π_1 and Π_2 .

Vortex-induced vibrations being another form fluid-structure interaction which occurs in a slender structure, has been investigated as candidate for power extraction from external flows. Significant progress on this problem have been made by Bernitsas et al. (2008, 2009); Raghavan and Bernitsas (2011); Lee and Bernitsas (2011) and other colleagues in VIVCACE group in the University of Michigan. Hence, it may seem that it is reasonable to present the data in a fluid-elastic problem using the same parameters in a VIV problem.

QSS data presented in figure 4.2 at $Re = 200$, shows a comparison between classical VIV and the newly formulated parameters presented as independent variables. The displacement amplitude, velocity amplitude and the mean power is presented in sub-figures (a), (c) and (e), as functions of the classical VIV parameter U^* for different ζ . The same data as functions of Π_2 , are presented in sub-figures (b), (d) and (f), for various, reasonably high values of Π_1 ($0.4 \leq \Pi_1 \leq 17.5$). Sub-figure (e) shows a similar trend to Barrero-Gil et al. (2010). The Value of the peak power remains constant. However, the power curve shifts to the right as ζ is increased. Here, in figure 4.2 the maximum dimensionless power is achieved at two times the velocity at which the galloping starts, which is similar to the observations made by Barrero-Gil et al. (2010); Vicente-Ludlam et al. (2014). An excellent collapse for velocity amplitude and mean power could be observed on the data, presented using the dimensionless group Π_2 , formulated using the natural time scales of the system. This implies that essentially velocity amplitude and the mean power is dictated by Π_2 which furthermore, implies that the natural frequency of the system which is used to scale U^* ,

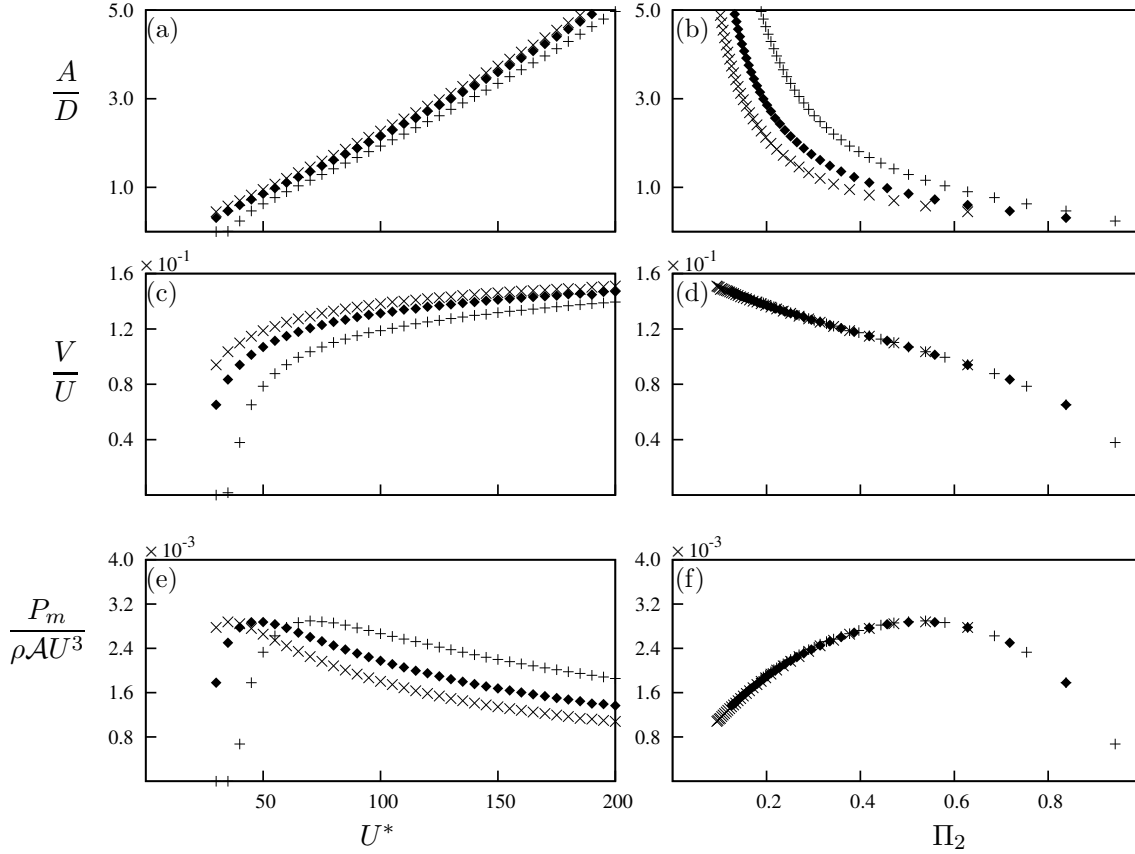


Figure 4.2: Displacement amplitude, velocity amplitude and dimensionless mean power data as functions of two different independent variables. Data presented in (a), (c) and (e) using the classical VIV parameter U^* , obtained at $Re = 200$ and $m^* = 20$ at three different damping ratios: $\zeta = 0.075$ (\times), $\zeta = 0.1$ (\blacklozenge) and $\zeta = 0.15$ (+). (b) (d) and (f) are the same data presented using the combined mass-damping parameter (Π_2) as the independent variable. Even though Π_1 varies in the range of $0.4 \leq \Pi_1 \leq 17.5$, it is clear that the power is a function of Π_2 only.

ζ and Π_1 does not have a significant influence on the behaviour of the system, unlike VIV, which is a resonant phenomenon.

4.3.2 High and low Re data

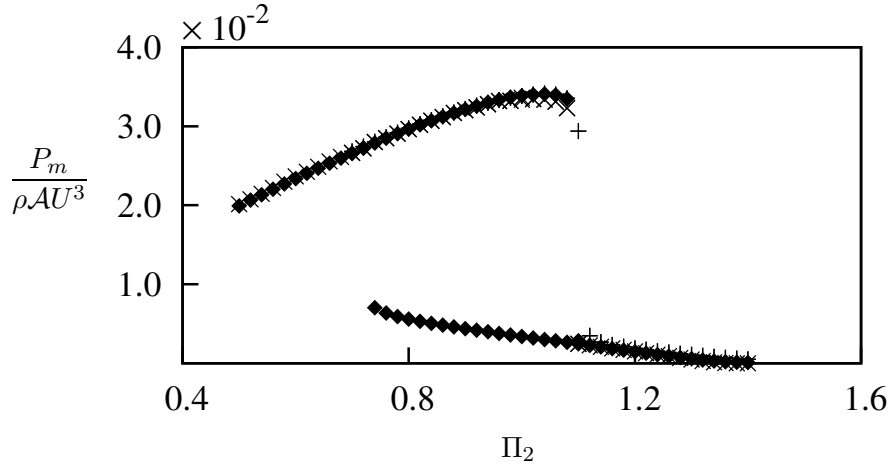


Figure 4.3: Dimensionless mean power as a function of Π_2 . Data presented at (a) $Re = 22300$, $\Pi_1 = 200$ (\times), $\Pi_1 = 2000$ (\blacklozenge) and $\Pi_1 = 10000$ ($+$). Hysteresis could be observed at high Re .

The successful collapse of data, mean power in particular using Π_2 for low Reynolds number ($Re = 200$), could be replicated at high Reynolds numbers. An example case is presented in figure 4.2 at $Re = 22300$ for selected values of Π_1 . The successful collapse of mean power data at high Reynolds numbers shows the suitability of using Π_2 as an independent variable across a large range of Reynolds numbers.

Hysteresis is evident in the high Reynolds number case ($Re = 22300$). Manipulating the initial condition (initial displacement) leads to obtaining different solutions for the same Π_2 value. The upper and lower branch were obtained by giving an initial displacement which was higher than the expected amplitude and providing a lower initial displacement respectively. Even though in theory, there is a possibility of a third state, this unstable branch could not be achieved with a time integration method (also observed by (Vio et al., 2007)) such as the one employed in this study.

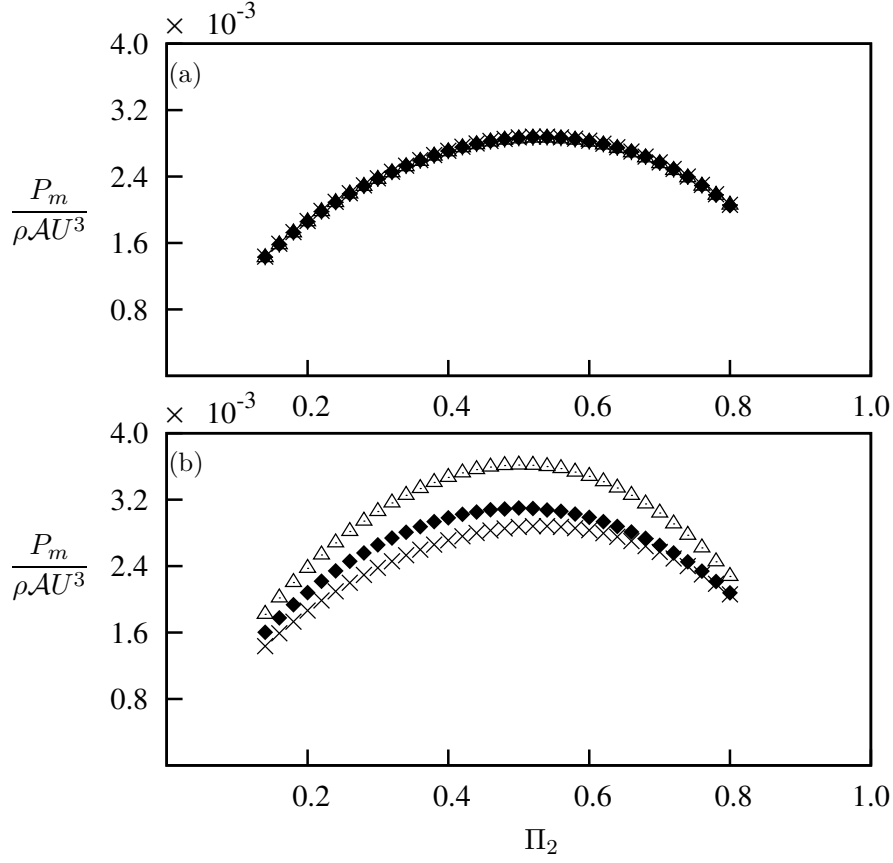


Figure 4.4: Dimensionless mean power as a function of Π_2 obtained using the QSS model at $Re = 200$. (a) High Π_1 ; data presented at four different combined mass-stiffness levels. $\Pi_1 = 10$ ($m^* = 20$, $U^* = 40$) (\times), $\Pi_1 = 100$ ($m^* = 80$, $U^* = 50$) ($+$), $\Pi_1 = 500$ ($m^* = 220$, $U^* = 60$) (\blacklozenge) and $\Pi_1 = 1000$ ($m^* = 400$, $U^* = 40$) (\triangle). (b) Low Π_1 ; data presented at $\Pi_1 = 10$ (\times), $\Pi_1 = 0.1$ (\blacklozenge), and $\Pi_1 = 0.01$ (\triangle).

4.3.3 Dependence on mass-stiffness, Π_1

From the results of sections 4.3.1 and 4.3.2 shows essentially a single variable governs the mean extracted power, which is the combined mass-damping parameter, Π_2 . The time scale analysis carried out in section 4.2 shows that not only Π_2 but also Π_1 influences the system. Previous studies such as Bouclin (1977) have also reported a complex interaction between the displacement amplitude and the natural frequency, for high natural frequencies in particular; or in this instance equivalent to low values of Π_1 . This section investigates the impact of Π_1 further. The overall behavior of the system is divided into two regimes, one for “high” Π_1 and the other for “low” Π_1 and analysed.

The mean power as a function of Π_2 for a range of values of Π_1 is presented in figure 4.4. In the two subfigures presented, (a) shows the data for $\Pi_1 \geq 10$, while (b) shows data for $\Pi_1 \leq 10$. The excellent collapse in figure 4.4(a) shows that for $\Pi_1 \geq 10$, the mean power is independent of Π_1 .

In contrast figure 4.4(b) shows that for low values of $\Pi_1 \leq 10$, the predicted mean power increases as Π_2 decreases. This indicates that at this region ($\Pi_1 < 10$), the mean power is a weak function of Π_1 ; hence, providing a distinction between high and low regimes of Π_1 . The mean extracted power is only a function of Π_2 where $\Pi_1 \geq 10$ or for high Π_1 . For low values, $\Pi_1 < 10$, the mean power becomes a strong function of Π_2 and a weak function of Π_1 .

It is clear that regardless of the value of Π_1 , the variation of power with Π_2 is essentially the same. As Π_2 is increased, the mean extracted power will increase to the point which, it will attain some maximum value and then decrease. This relationship between power and Π_2 could be explained by analysing the time histories of selected cases. AS an example, data at $\Pi_1 = 10$, $m^* = 20$ and $Re = 200$ are presented in figure 4.5. Three major regions where the value of the power curve are considered. These regions are Π_2 less than (region 1), equal to (region 2) and greater than (region 3) to the Π_2 value where the mean power is at its maximum.

The damping is low in region 1 ($\Pi_2 = 0.15$) in comparison with region 2 and 3. Although this may lead to larger oscillations, according to equation 3.1 damping is required to dissipate and therefore extract power. Hence, a low mean power output is gained at low damping. The high velocity amplitude leads the equivalent incident angle θ to exceed

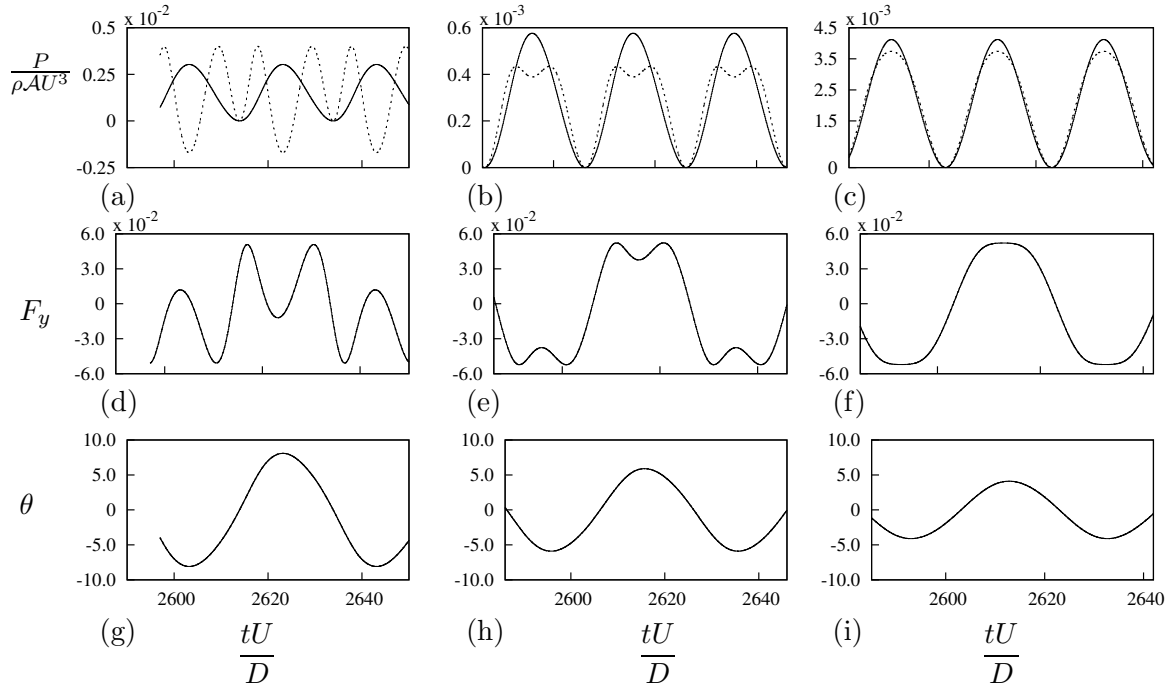


Figure 4.5: Time histories of P_t , P_d , F_y and θ at $\Pi_2 = 0.15, 0.54$ and 0.8 from the QSS model. Data was obtained at $m^* = 20$, $\Pi_1 = 10$ and $Re=200$. The time histories of P_d (—) and P_t (---) are presented for: (a) $\Pi_2 = 0.15$; (b) $\Pi_2 = 0.54$; (c) $\Pi_2 = 0.8$. Time histories of the instantaneous force F_y for: (d) $\Pi_2 = 0.15$; (e) $\Pi_2 = 0.54$; (f) $\Pi_2 = 0.8$. Time histories of the instantaneous angle θ for: (g) $\Pi_2 = 0.15$; (h) $\Pi_2 = 0.55$; (i) $\Pi_2 = 0.8$.

the positive range of C_y (i.e. $0 < \theta < 6^\circ$ as shown in figure 2.3(a)) resulting a negative transferred power by damping P_t over some portion of the cycle as shown in figure 4.5 (a). The galloping force F_y and the transverse velocity \dot{y} are not in phase in this portion of the cycle where the force opposes the direction of travel. As a consequence, during this period of time the opposite of what is expected happens, where the power is transferred from the structure to the fluid. Since Π_2 is substantially low, from an energy perspective, the mechanical damping is not sufficient to remove the energy transferred from the fluid to the structure through work during other times of the cycle. Hence, as depicted by the negative region of P_t , this excess energy is transferred back to the fluid.

A clear sinusoidal signal of both P_d and P_t (4.5(c)) could be observed at region 3 where $\Pi_2 = 0.8$ and the damping constant is high. The equivalent incident angle θ (which for small values, is proportional to the transverse velocity of the body) is in phase with the galloping force F_y as shown in figures 4.5(f) and 4.5(i). The velocity amplitude is small in this case resulting θ falling within the range where the fluid-dynamic force (F_y) increases within the incident angle (i.e. $0 < \theta \leq 5^\circ$ as shown in figure 4.1(a)). These conditions are favourable for high power output according to equation 3.2. Be that as it may, in this case the velocity is limited because of the high damping resulting relatively low fluid dynamic forcing.

A harmony between the high and low values of damping could be found at region 2 ($\Pi_2 = 0.54$). It is evident that P_t remains periodic but is not a pure sinusoidal signal. Two ‘peaks’ are present in a single half cycle from the time history graph of P_t as shown in figure 4.5(b). The velocity amplitude actually exceeds the equivalent incident angle where the fluid-dynamic forces peaks (i.e. $\theta = 5^\circ$ in 2.3 (a)) in this scenario. The dip in between the two peaks in a single half cycle correspond approximately to the time where the transverse velocity is higher than 0.09 and F_y is decreasing with increasing transverse velocity. As this region is the best compromise between region 1 and region 3, the maximum mean power could be attained in this region. Region 2 could also be identified as the “sweet spot” for energy extraction as the damping is high enough to obtain a high power output while not so high for the motion to be completely suppressed.

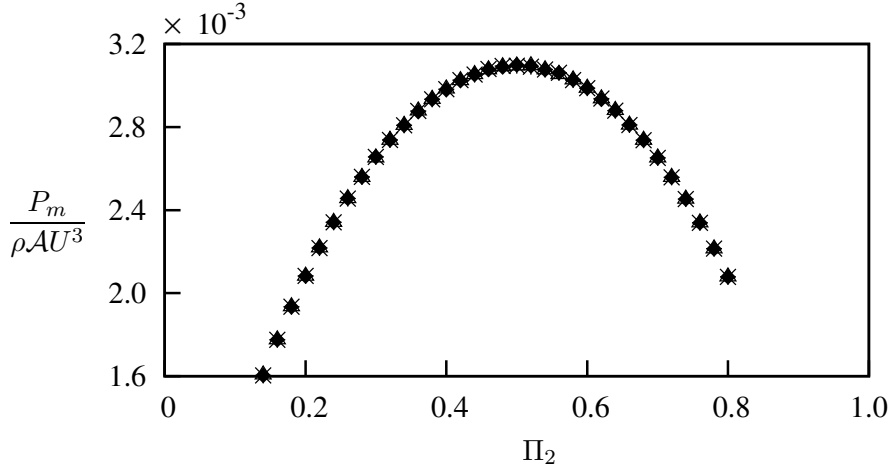


Figure 4.6: Dimensionless mean power as a function of Π_2 obtained using QSS model at $\Pi_1 = 0.1$. Data presented at $m^* = 2$ (\blacklozenge), $m^* = 20$ (\triangle) and $m^* = 50$ ($*$). The mass ratio does not have an effect on Π_1 even at low Π_1 .

4.3.4 Dependence on the mass ratio m^*

It is clear that the mean extracted power is only a function of Π_2 for high values of Π_1 . However, the question remains about the region of low Π_1 . Does the variation of the mean extracted power occur purely as a function of Π_1 , or does the mass ratio also has an influence on power? The QSS model was solved by varying the values for m^* but keeping the Π_1 fixed. In other words Π_1 was changed by changing the stiffness of the system.

It is clear from figure 4.6, data presented being the mean extracted power as a function of Π_2 , for a fixed $\Pi_1 = 0.1$, for three different values of m^* , that mean power is independent of m^* , hence, it is only a function of Π_1 and Π_2 .

4.3.5 Comparison with DNS data

The main drawback of the QSS model is that the instantaneous lift generated by the induced velocity is the only driving force of the system. However, in realistic scenarios the flow is far more complex and the only force affecting the system is not the induced lift. Force generated due to vortex shedding is one of the prominent forces in these systems. Hence, when the QSS model is being used, one of the essential assumptions is that the effect of vortex shedding is minimal. Due to this reason the model has been always used at high Reynolds numbers and at high m^* . Therefore, a study to identify the limiting parameters

of the QSS model at low Reynolds numbers was carried out using a comparison of QSS data with DNS results.

A sinusoidal forcing function was introduced to the QSS model in order to account for the forcing by vortex shedding by Joly et al. (2012). In this study displacement data obtained by the QSS model and the DNS simulations were compared which agreed well at low Reynolds numbers. The data were obtained at zero damping levels. As the primary focus of this study is the behaviour and the power transfer of the system, analysing the behaviour of the system with increasing damping is of interest.

Figure 4.7 provides a comparison between QSS and the DNS results. The maximum displacement, velocity and mean extracted power are presented as a function of Π_2 . A range of values of Π_1 are compared to the QSS model data for $\Pi_1 = 10$. Only little variation with Π_1 could be found in the displacement amplitude (figure 4.7(a)) and velocity amplitude (4.7(b)). Thus the comparison between the QSS model and the DNS simulation is quite satisfactory for these two quantities. In contrast, there is a significant influence of both Π_1 and Π_2 on the mean extracted power which is presented in figure 4.7(c). This discrepancy become more vivid in the regions where the value of Π_1 is low. These regions has the largest discrepancy between the QSS model and DNS data. A comparison of data between figures 4.7(c) and 4.4(a) shows that Π_1 has a much more significant influence on the extracted power than the predictions by the QSS model for low Π_1 values. Indeed as discussed in section 4.3.3 the QSS model predicts that the mean extracted power should increase with decreasing Π_1 when Π_1 moves to the low Π_1 region (figure 4.4(b)). However, the DNS data show sort of an opposite result where the extracted mean power decreases with decreasing Π_1 .

The dependence of the mean extracted power on Π_1 is clearly shown in figure 4.8(a). Here, the maximum power extracted for a given value of Π_1 , over all values of Π_2 (essentially the value of extracted power at the turning point), is plotted as a function of Π_1 . A quadratic fit was used obtain these values presented in figure 4.6 and finding the mean extracted power at the turning point of the power curve. It is clear that there is a rapid decrease in extracted power as $\Pi_1 \rightarrow 0$.

Figure 4.8(a) also shows that Π_1 is important to higher values than predicted by the QSS model. The maximum extracted power is essentially independent of Π_1 for $\Pi_1 > 10$,

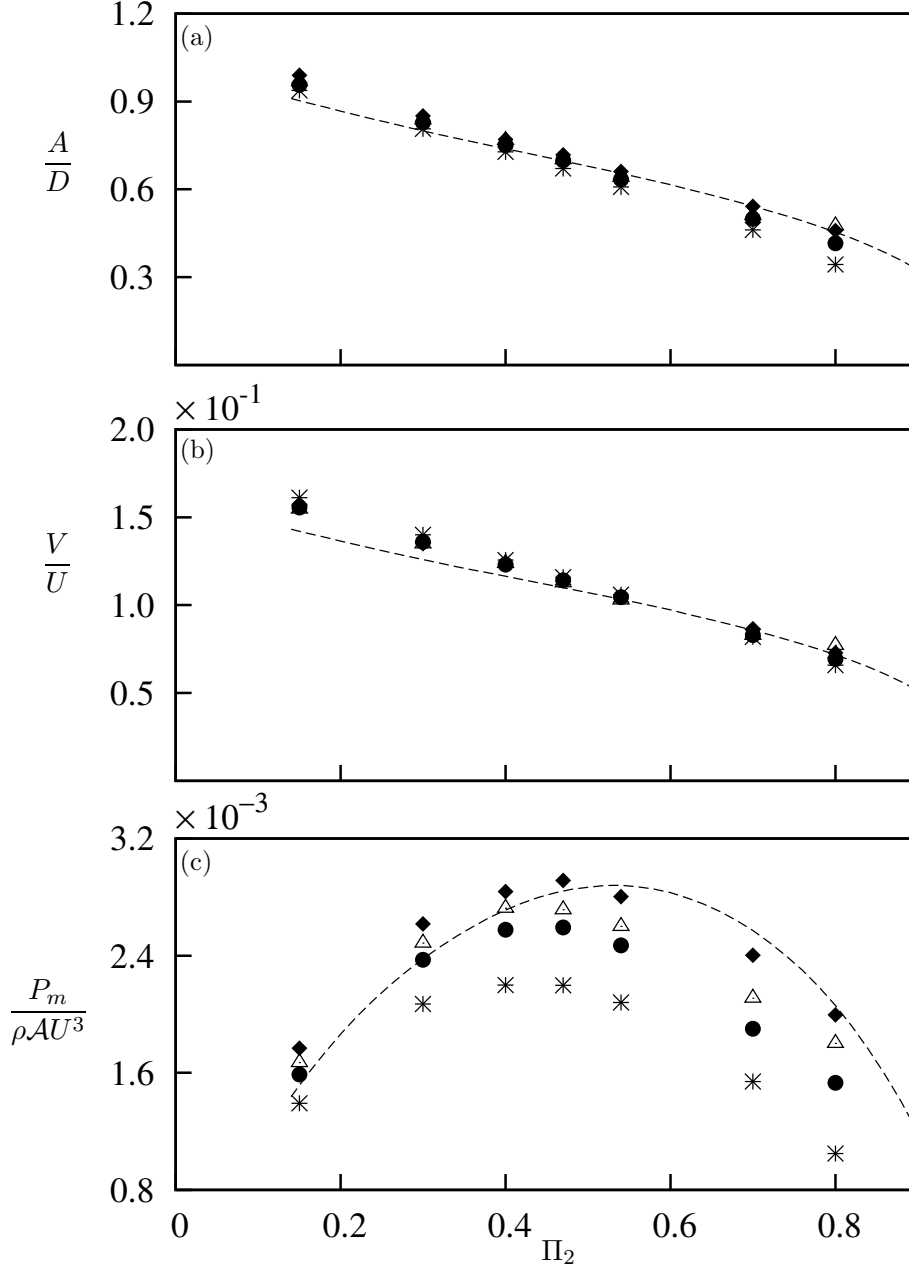


Figure 4.7: Comparison of data generated using the quasi-static model and full DNS simulations at (a) Displacement amplitude, (b) velocity amplitude and (c) dimensionless mean power as functions of Π_2 . Data were obtained at $Re = 200$ at four values $\Pi_1 = 10$ ($m^* = 20.13$) (*), $\Pi_1 = 60$ ($m^* = 49.31$) (●), $\Pi_1 = 250$ ($m^* = 100.7$) (△) and $\Pi_1 = 1000$ ($m^* = 201.3$) (◆). The QSS data at $\Pi_1 = 10$ (---).

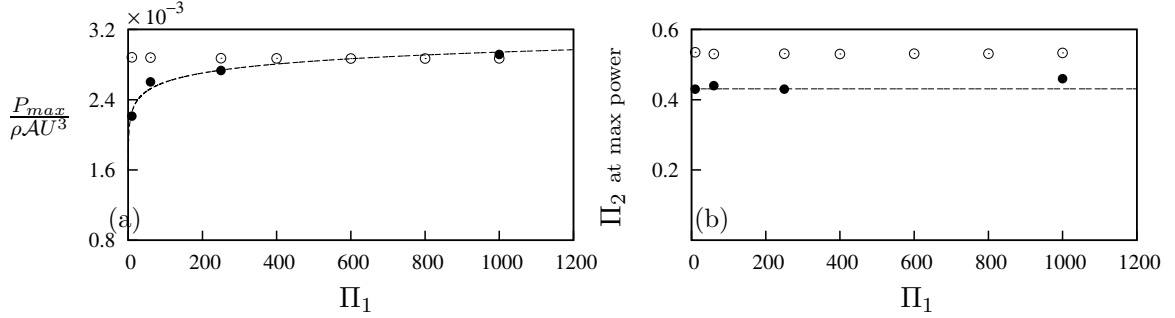


Figure 4.8: (a) Maximum power and (b) the value of Π_2 at maximum power of QSS data (○) and DNS data (●), as functions of Π_1 . For the DNS data, The maximum power asymptotes to an upper value with increasing Π_1 , while the value of Π_2 where maximum power occurs is relatively insensitive to Π_1 . The maximum power of the QSS data remains relatively constant, as does the value of Π_2 where maximum power occurs. The dash curve (---) of (a) follows the logarithmic fit of the maximum power which is $P_{max}/\rho AU^3 = 1.48 \times 10^{-4} \ln(\Pi_1) + 1.9 \times 10^{-3}$. The dashed curve in (b) shows the value $\Pi_2 \simeq 0.43$.

which could be observed by the open symbols in the figure. Nonetheless a significant dependence on Π_1 $\Pi_1 < 250$ could be observed in the extracted power. Yet, as the Π_1 increases the mean power converges to that of the values predicted by the QSS model.

The value of Π_2 at the turning point of the power curve or the point of maximum power is shown in figure 4.8(b). The open symbols represents the values predicted by the QSS model while the values predicted by DNS simulations are represented by the close symbols. These two values does not coincide where the DNS predictions (shown with a dashed line) has a value around 0.41 while the predictions of the QSS model has a value of 0.5. Regardless, both QSS model and DNS show that while the mean power is a reasonably strong function of Π_1 , the value of Π_2 at the point of maximum power output is relatively unaffected.

The percentage discrepancy between the QSS DNS extracted power data as a function of Π_1 was calculated using equation 4.9 in order to further quantify the performance of the QSS model.

$$\% \text{ error} = \left| \frac{P_{m(QSS)} - P_{m(DNS)}}{P_{m(DNS)}} \right| \times 100. \quad (4.9)$$

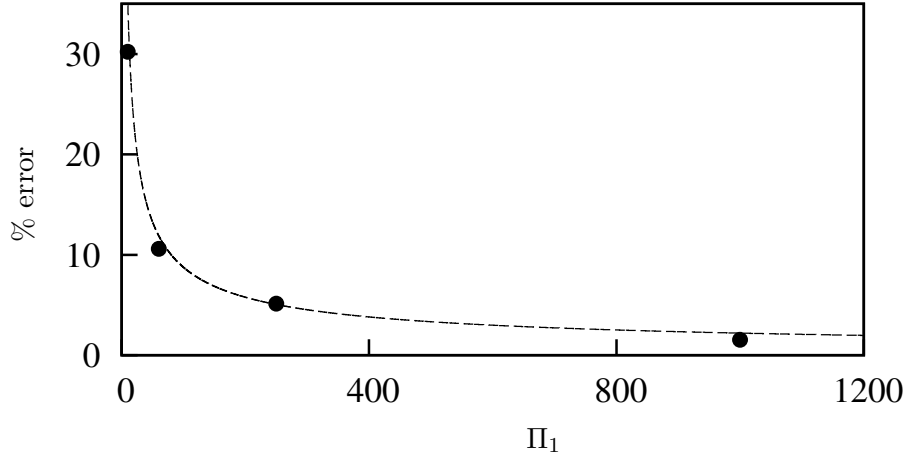


Figure 4.9: The percentage error between the maximum power obtained using DNS data and predicted by QSS model as a function of Π_1 . The QSS model prediction is worst for low values of Π_1 . The dash curve (---) follows the power law fit of the percentage error which is $\%error = 138.697\Pi_1^{-0.6}$.

Figure 4.9 shows the data obtained by this error calculation along with a power-law best fit $138.697\Pi_1^{-0.6}$. It clearly shows that as Π_1 increases the percentage error between QSS model and DNS quickly decreases. But, the discrepancy between the two can be quite large, about 30% at low values of Π_1 .

The influence of vortex shedding could be one of the likely reasons for this discrepancy at low Π_1 which is not accounted for in the QSS model. The frequency spectra of the velocity of the body from DNS cases at varying Π_1 at a value of $\Pi_2 = 0.47$ which is close to the value at which the mean extracted power is a maximum, were plotted to test this hypothesis. Figure 4.10 shows this power spectrum plots along with the original time histories of the transverse velocities of the body.

This figure shows the velocity signals at $\Pi_1 = 0.8$ and $\Pi_2 = 10, 60, 250$ and 1000 and the corresponding spectrum. A significant component around $fd/U = 0.156$ which can be identified as the vortex shedding frequency could be seen in the spectral data. As Π_1 increases a clear reduction of the magnitude of the component at the vortex shedding frequency could be observed. This indicates that the influence of vortex shedding is much more prominent at low Π_1 , therefore resulting in larger deviations from quasi-steady state results. This builds on the work of Joly et al. (2012), which was conducted at zero damping,

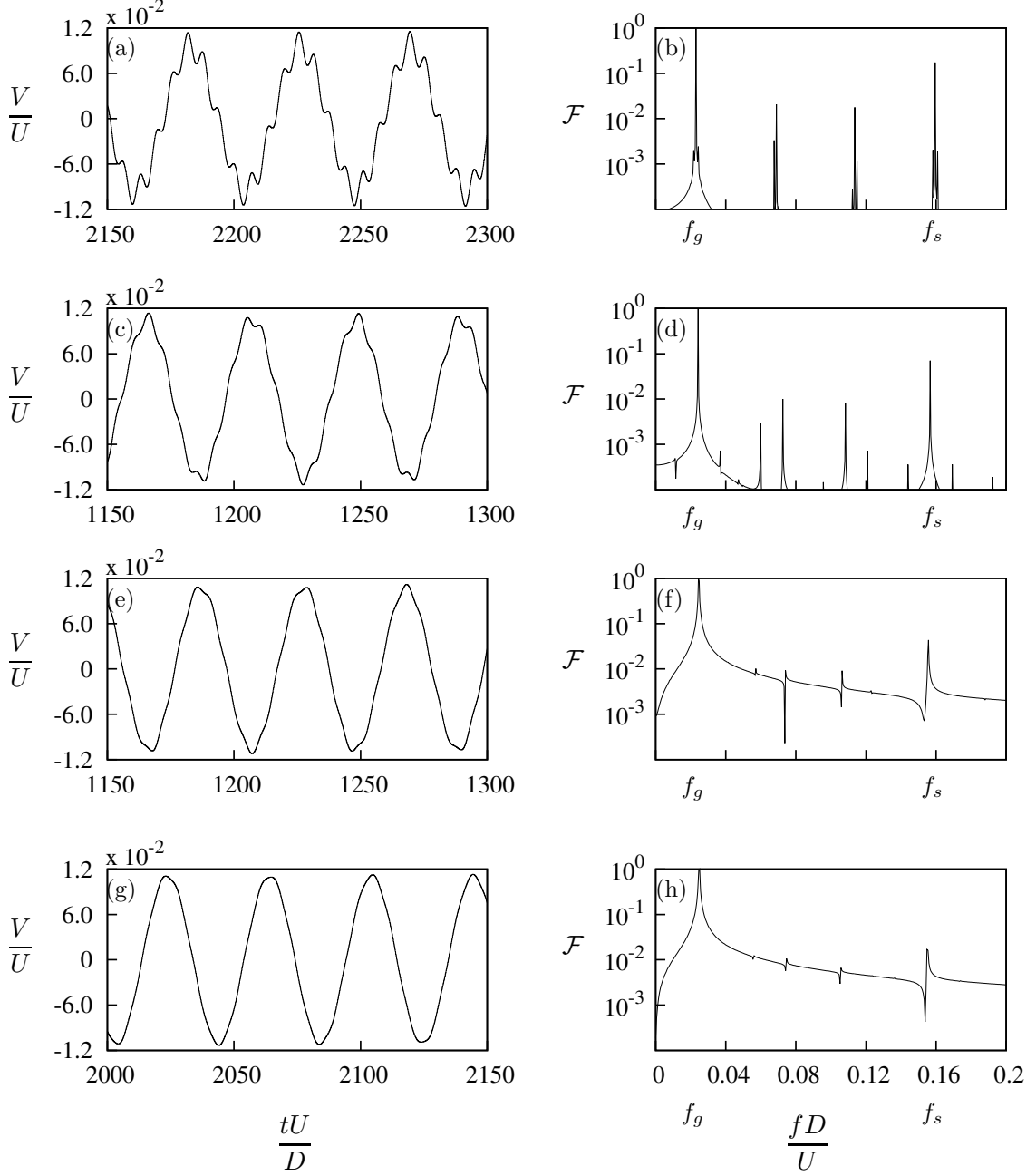


Figure 4.10: Velocity signal (right) and the corresponding power spectrum (left) of the DNS data at four values of Π_1 at $\Pi_2 = 0.47$. (a) and (b) $\Pi_1 = 10$, (c) and (d) $\Pi_1 = 60$, (e) and (f) $\Pi_1 = 250$, (g) and (h) $\Pi_1 = 1000$. U^* is kept at 40 therefore the mass ratio increases as Π_1 increases. It is evident that the influence of vortex shedding reduces as the inertia of the system increases.

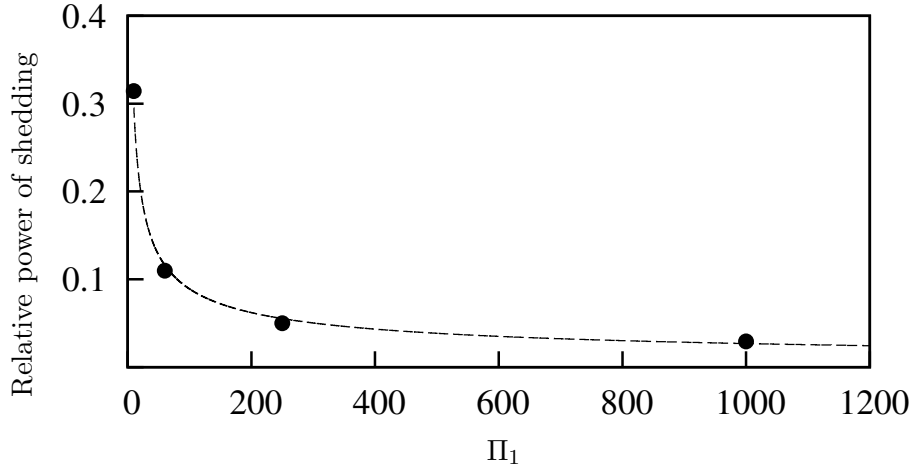


Figure 4.11: The relative power of the vortex shedding as a function of Π_1 . The relative power of the vortex shedding decreases as Π_1 increases. The dash curve (---) follows the power law fit of the percentage error which is $\text{Relative power} = 0.977\Pi_1^{-0.52}$.

that implied that mean extracted power would be influenced by vortex shedding at low mass.

This influence is explicitly shown here. Figure 4.11 plots the relative intensity of the component at the vortex shedding frequency to the component at the galloping or oscillation frequency in the spectra of figure 4.10.

The relative strength of the vortex shedding is seen to be large at low values of Π_1 and drastically decreases as Π_1 is increased. This follows a similar behaviour to the discrepancy between the QSS and DNS mean extracted power shown in figure 4.9. From the figure to could be seen that the variation of the relative power of the vortex shedding frequency to the galloping frequency is similar to $0.977\Pi_1^{-0.52}$

The difference between the power predicted by the QSS and DNS models scales with $\Pi_1^{-0.6}$ while the relative power at the vortex shedding frequency scales with $\Pi_1^{-0.52}$. Both these scalings are quite similar which is closer to $1/\sqrt{\Pi_1}$. Though it is unequivocal, this correlation is a strong indication that the discrepancy between QSS and DNS is result of the influence of vortex shedding, even though the frequencies of vortex shedding and galloping remains well separated by around similar amount for all values of Π_1 (Figure 4.11). The data presented in figure 4.11 also give some sort of an indication of the strength of any vortex shedding correction term that might be added to the QSS model in an effort to decrease

the discrepancy between it and the DNS simulations.

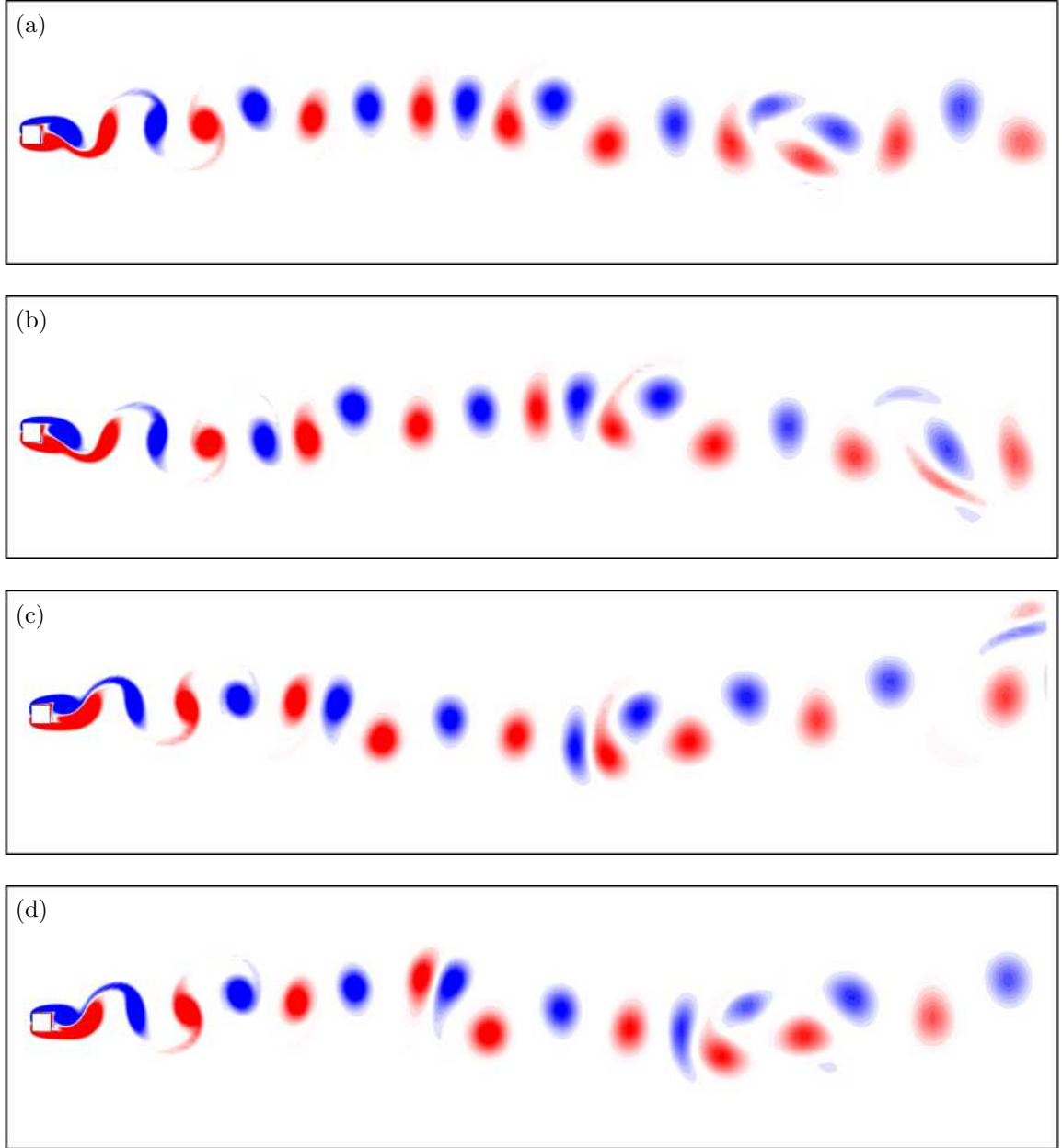


Figure 4.12: Vorticity plots of the flow at arbitrary instants at $\Pi_2 = 0.47$. (a) $\Pi_1 = 10$, (b) $\Pi_1 = 60$ (c) $\Pi_1 = 250$ and (d) $\Pi_1 = 1000$ at $Re = 200$. Contours show vorticity at levels between ± 1 .

More information can be gained by analysing the flow field. Figure 4.12 shows the flow field data at arbitrary instances where the values of Π_2 are close to the point of

the maximum power at different Π_1 a clear wavelength could be observed in this figure. Qualitatively, this can be interpreted as such that at high Π_1 , the vortex shedding is simply superimposed over the path of motion of the cylinder. A decrease in amplitude of this wave could be observed at low Π_1 which may be caused due to the higher levels of non-linear interactions between vortex shedding and galloping. Such an argument is constant with the data of figure 4.11 that show the increasing significance of vortex shedding as Π_1 decreases. Bundled together, this also to a certain extent helps to explain the discrepancy between the mean extracted predicted by the QSS and DNS models at low Π_1 , highlighted in figure 4.9.

4.4 Summary of the governing parameters of fluid-elastic galloping

An analysis of the power transfer of a square body under fluid-elastic galloping is presented in this chapter. This analysis was carried out by solving the quasi-steady state oscillator model equation with the use of numerical integration. Dimensionless groups were formulated by through the relevant time scales by linearising the QSS equation. In comparison with classical VIV parameters i.e. ζ and U^* a good collapse could be obtained with these newly formulated parameters. Having the collapsed data using the dimensionless groups further strengthens the argument that the velocity amplitude and the power transfer of the system does not depend on the natural frequency of the system over a large range of natural frequencies.

Although m^* is shown to be an independent parameter in equation 4.8, the results show that the system is only a function of Π_1 and Π_2 essentially. This could be explained by inspecting equation 4.8, which shows that m^* only has an impact on the forcing terms which are non-linear in relation to the velocity of the body. In order for these terms to be appreciable, the velocity of the body, and hence, the induced angle of attack need to be quite high, which for the range of parameters tested here, appears not to be the case.

Comparing with direct numerical simulation data, the quasi steady state model provide a good approximations of the power output when the Π_1 of the system is relatively large. But, at low values of Π_1 , the prediction has a large discrepancy, as the QSS model does

not account for the impact of vortex shedding, where the influence increase as the Π_1 is decreased. That being said, the QSS model does provide quite a reasonable prediction of the value of Π_1 at the point where the maximum power is produced. Both the error in predicted maximum power between the QSS and the DNS models, and the relative power of the vortex shedding, have been quantified. It scale similarly to $1/\sqrt{\Pi_1}$.

The presence of a clear wave length in the flow field at high Π_1 and the reduction of this wavelength as Π_1 decreases provides more evidence to the fact that vortex shedding has a complex influence on galloping systems.

CHAPTER 5

FREQUENCY RESPONSE OF THE SYSTEM

5.1 Introduction

The new governing parameters (Π_1 and Π_2) formulated using the linearised QSS equation in chapter 4 provide a good representation of velocity amplitude and mean power output. In this chapter, the new governing parameters are further analysed by investigating the impact of these parameters with galloping frequency response.

This chapter is quite brief as it was not the primary objective of this study. However, the investigation into the frequency behaviour was carried out to compliment the understanding of Π_1 and Π_2 on galloping.

The flow of this chapter is as follows. An expression for the frequency is formulated based on Π_1 and Π_2 through the natural time-scales of the system. Data are obtained for frequency by pushing the models to the extreme end in order to find limits where it provides an accurate approximation. This followed by the presentation of results through plots and contour plots in Π_1 and Π_2 space. Finally the limits of the formulated equation is identified and conclusions are made on the galloping frequency.

5.2 Formulating the linear frequency of the system

The process was initiated by considering the linearised galloping equation (Eq:4.1). The eigenvalues of the linearised QSS model could be found in equation 4.2. The term under the square root (equation 5.1) of this equation can be used to express the frequency of the system provided that the eigenvalues are complex.

If this condition (presence of complex eigenvalues) is satisfied, the imaginary component could be identified as the frequency of the system.

$$f = \sqrt{\left[\frac{c - \frac{1}{2}\rho U A a_1}{(m)} \right]^2 - 4 \frac{k}{(m)}}. \quad (5.1)$$

By substituting c^* , m^* and U^* equation 5.1 could be non-dimensionalised as follows:

$$f = \sqrt{\left[c^* \left(\frac{U}{D} \right) - \frac{1}{2} \frac{a_1}{m^*} \left(\frac{U}{D} \right) \right]^2 - 4 \left(\frac{U}{D} \right)^2 \frac{2\pi}{U^*}}. \quad (5.2)$$

This can then be rewritten as

$$f = \sqrt{\left(\frac{U}{D} \right)^2 \left(c^* - \frac{a_1}{2m^*} \right)^2 - 4 \left(\frac{U}{D} \right)^2 \left(\frac{2\pi}{U^*} \right)^2}. \quad (5.3)$$

By taking the factor of U/D to the left-hand side

$$\frac{fD}{U} = \sqrt{\left(c^* - \frac{a_1}{2m^*} \right)^2 - 4 \left(\frac{2\pi}{U^*} \right)^2}. \quad (5.4)$$

Expanding terms gives

$$\frac{fD}{U} = \sqrt{c^{*2} - \frac{2c^*a_1}{2m^*} + \frac{a_1^2}{4m^{*2}} - \frac{16\pi^2}{U^{*2}}}. \quad (5.5)$$

Multiplying through by m^{*2} gives

$$\frac{fD}{U} = \sqrt{c^{*2}m^{*2} - c^*m^*a_1 + \frac{a_1^2}{4} - \frac{16\pi^2m^{*2}}{U^{*2}}}. \quad (5.6)$$

By substituting Π_1 and Π_2 appropriately the expression of the linear frequency reduced to

$$\frac{fD}{U} = \sqrt{\Pi_2^2 - \Pi_2 a_1 + \frac{a_1^2}{4} - 4\Pi_1}. \quad (5.7)$$

Thus, from equation 5.7 the non-dimensionalised linear frequency of the system could be expressed from the newly formulated terms, Π_1 and Π_2 .

5.3 Frequency data

The limiting factor of this equation is the instance where it becomes a real number. Thus, certain questions arise. Does the QSS model predict a frequency beyond this point ?, i.e. after eq:5.7 becomes real. If so, what governs the frequency ? Is this region realistic ? or in other words could this region be identified through DNS simulations.

5.3.1 Comparison of all types of frequencies

Using different techniques three types of frequencies were found namely f_{lin} , f_{QSS} and f_{DNS} . For a give value of Π_1 and Π_2 the linear frequency f_{lin} was found by solving equation 5.7. f_{QSS} was obtained by performing an power spectrum analysis on the output signal of the velocity obtained by numerically solving the quasi-steady state equation. f_{DNS} was obtained using the similar technique as f_{QSS} but the velocity data was obtained through DNS simulations of fluid-structure interactions.

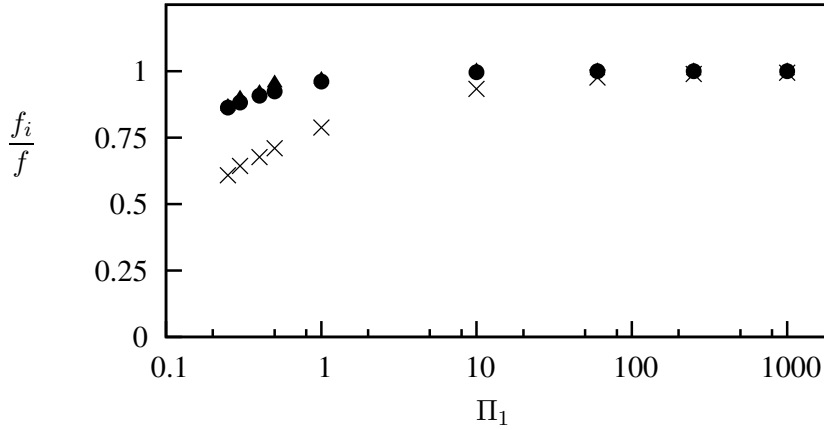


Figure 5.1: Frequency ratio as a function of Π_1 . Frequency obtained using QSS simulations, DNS simulations and the linear frequency equation (Eq:5.7) normalised by the undamped natural frequency f . f_i is the type of frequency i.e. $f_{DNS}, f_{QSS}, f_{lin}$. Data present $\frac{f_{lin}}{f}$ (●), $\frac{f_{QSS}}{f}$ (▲) and $\frac{f_{DNS}}{f}$ (×) at $\Pi_1 = 0.15$, $Re = 200$ and $f = 0.025$

The different frequencies normalised by the undamped natural frequency f as a function of Π_1 is presented in figure 5.1. It is to be noted that the undamped natural frequency was kept constant at $f = 0.025$. The frequency obtained using DNS f_{DNS} is the first to deviate

followed by f_{QSS} and then f_{lin} . The early deviation of f_{DNS} could be due to the non linear interaction between the galloping and other forms of forcing such as vortex shedding.

Given the circumstances two regions of frequency response could be identified namely, the linear region where a $f_{lin} > 0$ and the non-linear region where $f_{lin} = 0$. The data of these two regions are discussed separately.

5.3.2 Linear frequency region

Figure 5.1 shows the frequency ration between f_{lin} and f_{QSS} at the region where $f_{lin} > 0$.

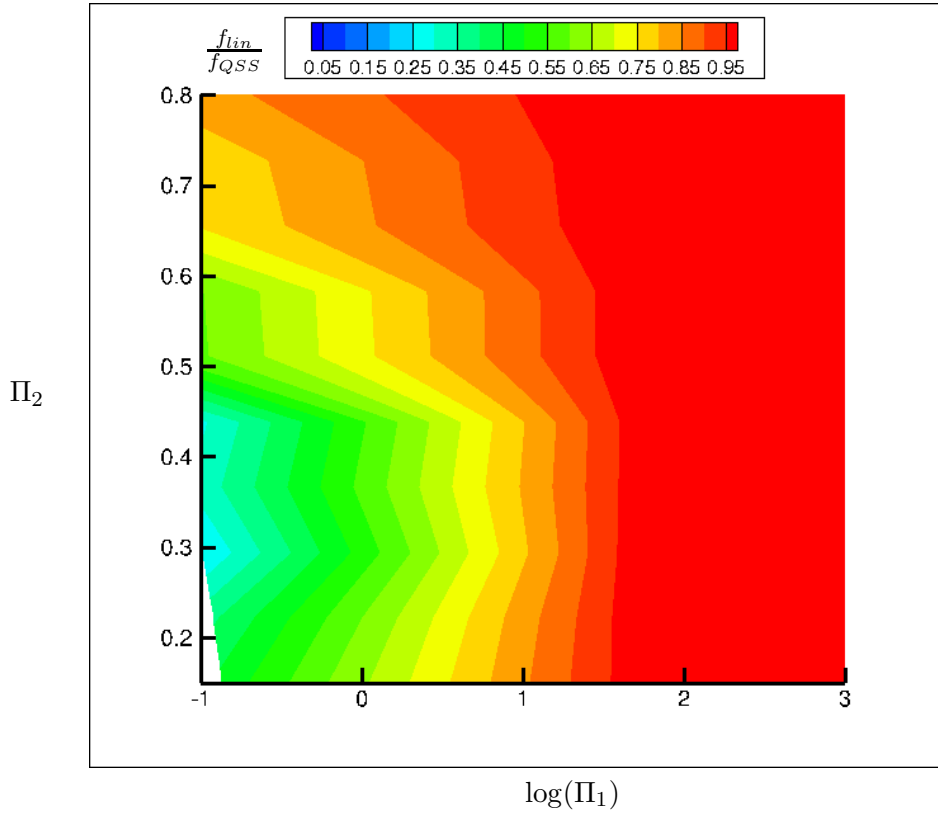


Figure 5.2: Contour plot of $\frac{f_{lin}}{f_{QSS}}$ in $\log(\Pi_1)$ Π_2 space. The linear frequency f_{lin} provides a good agreement with the frequency predicted by the quasi-steady state model beyond $\Pi_1 = 10$

The QSS frequency data tends to agree well between f_{lin} and f_{QSS} until $\Pi_1 = 10$ for almost all values of Π_2 . As Π_1 is further reduced the frequency ratio tends to reduce implying a further deviation between the frequencies.

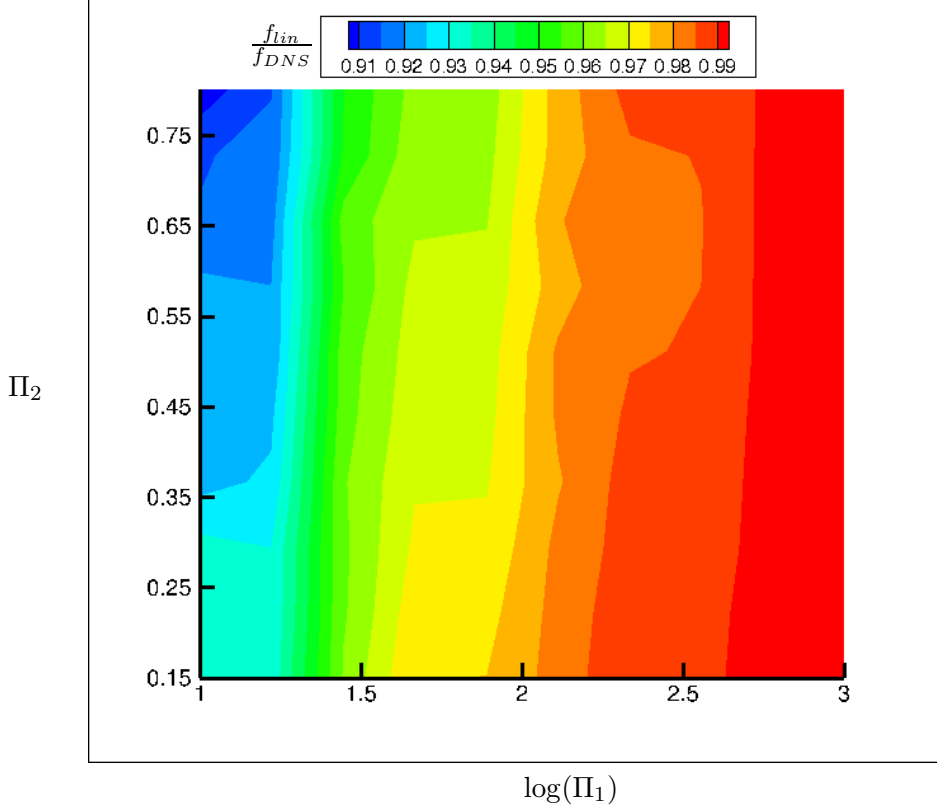


Figure 5.3: Contour plot of $\frac{f_{lin}}{f_{DNS}}$ in $\log(\Pi_1)$ Π_2 space. The linear frequency f_{lin} provides a good prediction of the DNS frequency over the range of Π_1 selected.

This pattern could also be observed for the DNS data (figure 5.3). The two frequencies f_{lin} and f_{DNS} tend to have a good agreement in the selected space of Π_1 and Π_2 . It should be specially noted that the lower boundary of Π_1 was limited ($\Pi_1 = 10$) because of the fact that galloping was weak in the DNS data hence, no galloping frequency could be obtained with the power spectrum analysis. However, there could be other techniques which was not considered here as mentioned earlier this analysis was a brief study to complement the understanding of Π_1 and Π_2 .

5.3.3 Non-linear frequency region

Non-linear frequency region is categorised as the region where no linear frequency is predicted or in other words $f_{lin} = 0$. Even though there was no linear frequency predicted the QSS model provided a signal for velocity and displacement and therefore providing a

frequency.

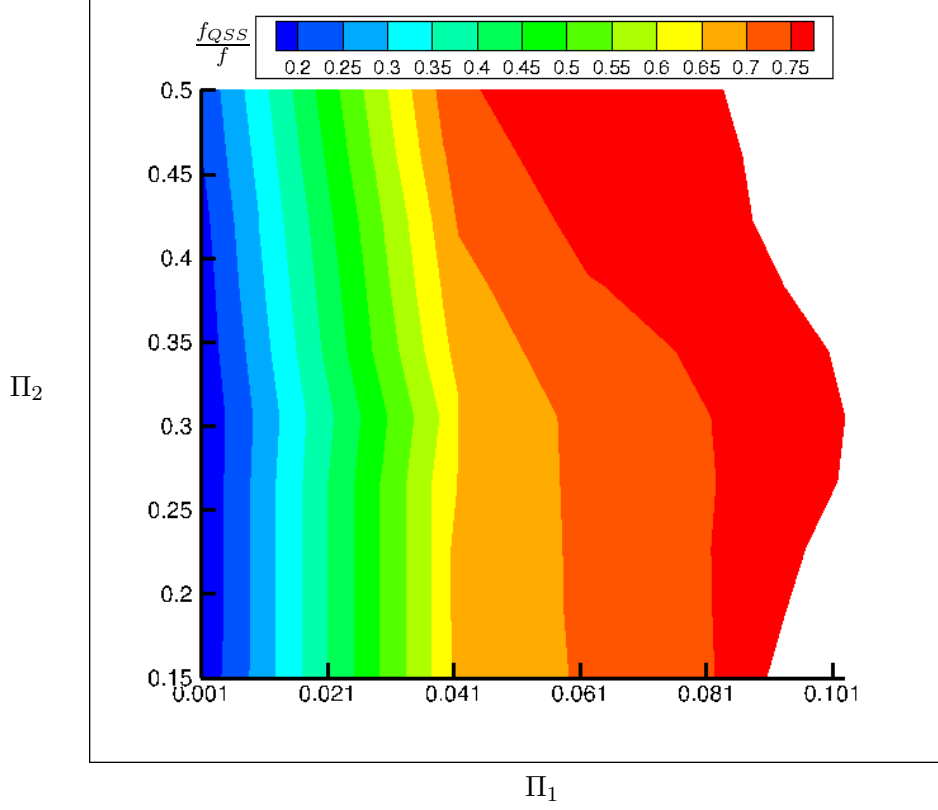


Figure 5.4: Contour plot of $\frac{f_{QSS}}{f}$ in Π_1 Π_2 space, at the region where no linear frequency is predicted ($f_{lin} = 0$).

The frequency ratio $\frac{f_{QSS}}{f}$ tends to deviate as Π_1 reduces (Figure 5.4) implying more influence of the non-linear terms of the forcing. This region is where the QSS model was pushed to the very extreme end where very large values of U^* was observed ($m^* = 20$ was kept constant).

It is to be noted that this non-linear region may not be practical and hence, may not be able to achieve from DNS simulations. Be that as it may, an in-depth analysis should be carried out using some other technique to isolate the weak galloping signal to back this argument. In the current study this was not carried out due fact that it is slightly out of the main scope of the main study and time constrains.

5.4 Summary of the frequency response of the system

An expression for the frequency of the system was formulated in terms of Π_1 and Π_2 together with the eigenvalues of the system. The frequency obtained using this expression was termed linear frequency or f_{lin} . Two frequency regions were identified namely the linear frequency region and the non-linear frequency region. The linear-frequency region was the region in Π_1 and Π_2 space where $f_{lin} > 0$ and the non-linear region was where $f_{lin} = 0$. The linear frequency agreed well with the DNS results within the boundaries used in the linear frequency region. The lower boundary of Π_1 was limited to $\Pi_1 = 10$ as galloping got weaker and vortex shedding got more prominent. The QSS results agreed well for higher values of Π_1 in the linear frequency region but tends to deviate as Π_1 was reduced.

QSS frequency was compared with the undamped natural frequency of the system f , in the non linear region. This revealed that it had a acceptable agreement with undamped natural frequency of the system in the rage of $0.06 \leq \Pi_1 \leq 0.1$ and tends to deviate as Π_1 reduced.

The mere existence of this region was a question as no DNS data could be obtained in this region due to the fact that galloping signal was weak and the techniques used to obtain the frequency was not sensitive enough to capture these weak signals. Thus it was concluded that further investigations should be carried out on this region but was not pursued in this study due to deviation of the major objective and scope and time constrains.

Be that as it may, The linear expression provided a excellent prediction within the boundaries where DNS data were obtained and therefore complimenting the understanding of the new formulated parameters Π_1 and Π_2 .

CHAPTER 6

INFLUENCE OF FLUID DYNAMICS OF THE SYSTEM ON THE EXTRACTED POWER

6.1 Introduction

This chapter contains the results and discussion relating to the third objective of this thesis. As discussed in chapter ?? the induced force F_y of the system is a result of the top and bottom of the shear layer behaviour of the system. The current published work shows that the afterbody of the system has a significant influence on the galloping response. In this chapter, the influence of shear layer behaviour and hence, the influence of the afterbody on mean extracted power is discussed.

Here, the influence of shear layer on the mean power is studied by introducing a cross section which is a hybrid of a square and a triangle. Data are analysed the cross section is transformed gradually by manipulating the ratio of two length scales.

The stationary forcing data is presented for each cross section followed by the QSS power curves. Based on the QSS power data, an optimum cross section for power extraction is identified. Next, the underpinning reason for the negative portion of certain C_y curves is discussed through surface pressure and flow velocity data. Following this, a reasoning for the discrepancy between QSS and DNS mean power at the optimum power cross section is

discussed.

A final summary is presented explaining the influence of the shear layer on mean power output and the preliminary design considerations to optimise the fluid mechanics to obtain an optimum power output.

6.2 Influence of the shear layers

As highlighted in section ?? the afterbody of the cross section has a significant influence on galloping. This is because of the shear layer need to interact with the afterbody after separation at the leading edge.

The C_y vs α curve increases reaches a maximum and reduces as the induce angle is increased. The maximum of the induced lift occurs when the separated shear layer (at the leading edge) closer to the surface of the body reattaches at the trailing edge. Therefore, by delaying the reattachment the point where the maximum lift occurs can be shifted towards a higher induced angle which leads to a higher induced velocity. As shown in equation 3.2 higher velocity leads to higher power output. In order to test this hypothesis the shear layer reattachment was reduced by gradually tapering off the top and bottom sides of the square cross section as sown in figure 6.1. The $\frac{d}{l}$ was changed gradually from 1 to zero at increments of 0.25 where 1 being the square cross section and 0 being an isosceles triangle.

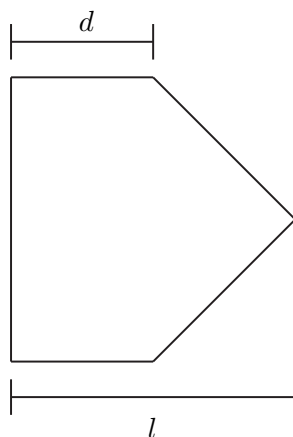


Figure 6.1: Illustration of the hybrid cross section (combination of a square and a triangle) obtained by tapering the afterbody of the square. The afterbody was changed by changing the ratio of $\frac{d}{l}$. Hence, data were obtained for $\frac{d}{l} = 1, 0.75, 0.5, 0.25$ and 0.

6.3 Static body results

$\frac{d}{l}$	a_1	a_3	a_5	a_7	
0	-2.30617	-269.075	-59.2929	4.74389	20.5° – 23.5°
	-5.08342	-56.5390	-160.505	-105.773	28.6° – 28.7°
	4.40685	19.9213	22.8894	7.68556	
0.25	-0.605146	-19.4346	-82.4463	-94.4226	30.1° – 30.2°
	2.50538	9.91021	10.2712	3.94112	
0.5	1.44734	4.83885	-166.900e	-983.072	14° – 16°
	1.51455e	15.8476	52.5465	62.8067	
0.75	1.76938	35.2630	-345.562	-10072.7	11.03° – 11.11°
	1.77553	43.0120	262.983	638.484	

Table 6.1: Coefficient values used in the 7th order interpolation polynomial at $Re = 200$. Data present for $\frac{d}{l} = 0 - 0.75$ at increments of 0.5. Multiples polynomials were used to attain a better fit. The plot of the compound fit is presented in figure 6.2.

Stationary C_y results were obtained for cross sections where $\frac{d}{l} = 1, 0.75, 0.5, 0.25, 0$. Where $\frac{d}{l} = 1$ being the square and $\frac{d}{l} = 0$ being an isosceles triangle. Table 6.1 shows the coefficients of the 7th order interpolation polynomial for each cross section. In order to achieve a better fit, piecewise interpolation using multiple 7th order polynomials were incorporated for a single cross section. During the curve fitting process more importance

6. INFLUENCE OF FLUID DYNAMICS OF THE SYSTEM ON THE EXTRACTED POWER

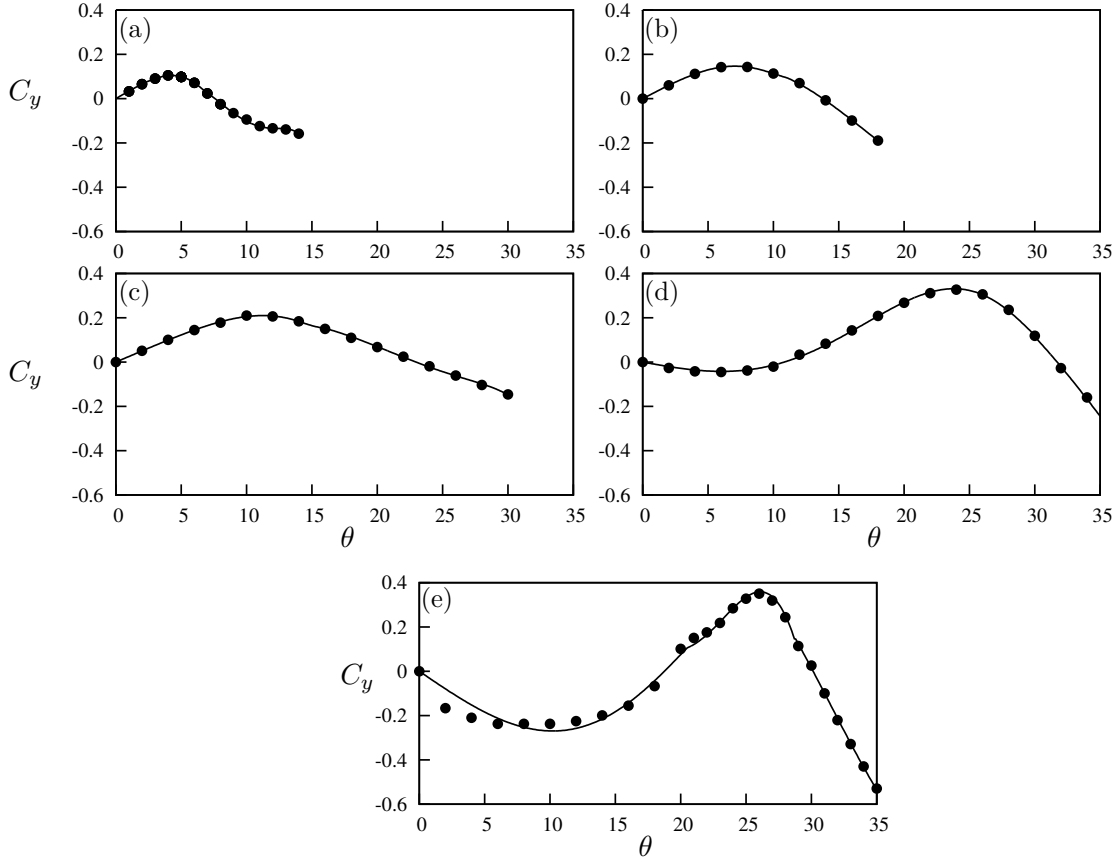


Figure 6.2: Induced lift coefficient C_y at different angles for selected cross sections. Data presented for cross sections, (a) square, (b) $\frac{d}{l} = 0.75$, (c) $\frac{d}{l} = 0.5$, (d) $\frac{d}{l} = 0.25$ and (e) triangle. Points (\bullet) are measurements from the static body simulations and the curves are the compound 7th order polynomials.

was given to the positive portion of the C_y curve as this portion of the data ensures that the galloping is sustained.

The C_y vs. θ curves in figure 6.2 shows that the peak value of C_y shifts to the right as $\frac{d}{l}$ is increased. These data agree with (Luo et al., 1994) where the peak of the maximum C_y value was shifted to higher induced angles when reattachment was delayed. As θ is proportional to the transverse velocity of the body $\tan\theta = \frac{\dot{y}}{U}$, it is clear that the maximum C_y occur at higher velocities as $\frac{d}{l}$ is decreased which was an expected outcome. Another interesting observation is that the presence of a negative portion prior to the point of maximum C_y in the C_y vs. θ curves as $\frac{d}{l}$ is decreased. In this region, C_y decreases reaches a minimum and then increases as θ is increased. The absolute value of the maximum is

grater than the absolute value of the minimum. This negative portion starts to emerge at $\frac{d}{l} = 0.25$. However, the maximum value of C_y increases as $\frac{d}{l}$ is decreased providing an indication of a possibility of attaining a higher power output at low $\frac{d}{l}$.

Yet, it is to be noted that the presence of the negative portion of the lift curve will oppose the motion of the body where the velocity of the body and the driving force will be out of phase. This will lead to an energy transfer from the body to the fluid which is the opposite of the expectations resulting a reduction in mean power output.

6.4 QSS results

6.4.1 Mean power output

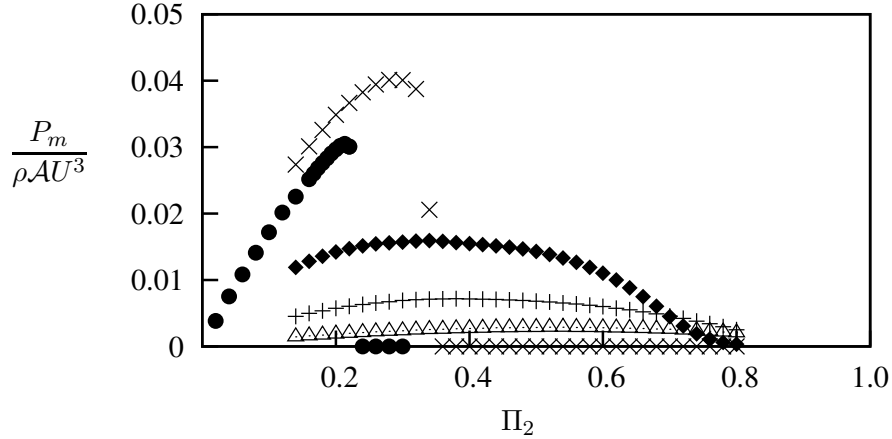


Figure 6.3: Dimensionless mean power obtained using QSS model as a function of Π_2 . Data presented for five selected cross sections, square (\triangle), $\frac{d}{l} = 0.75$ (+), $\frac{d}{l} = 0.5$ (\blacklozenge), $\frac{d}{l} = 0.25$ (\times) and triangle (\bullet) at $Re = 200$, $\Pi_1 = 100$.

Figure 6.3 shows the mean power Π_2 vs. mean power for different cross sections namely $\frac{d}{l} = 1, 0.75, 0.5, 0.25$ and 0 . The shear layer reattachment is decreased as $\frac{d}{l}$ is decreased. The mean power increases as $\frac{d}{l}$ is decrease where a significant increase in the maximum power could be observed. This meets the expectations where it was hypothesised that the mean power would increase as the shear layer re-attachment is delayed. A rapid increase in mean power could be observed below $\frac{d}{l} = 0.5$.

As $\frac{d}{l}$ decreases beyond 0.25 , as the mean power reaches the maximum a sudden drop

6. INFLUENCE OF FLUID DYNAMICS OF THE SYSTEM ON THE EXTRACTED POWER

could be observed as Π_2 is increased (eg. $\Pi_2 = 0.39$ for $\frac{d}{l} = 0.25$). One interesting fact which could be observed is that the maximum power at $\frac{d}{l} = 0.25$ is larger than $\frac{d}{l} = 0$. This is against the expected outcome as the hypothesis was that by delaying the shear layer reattachment a higher mean power output could be gained.

It is clear that as discussed in section 6.3 the negative portion of the C_y curve influences this reduction in maximum power at $\frac{d}{l} = 0$ in comparison with $\frac{d}{l} = 0.25$. Comparing the initial negative portion of the C_y vs θ plot of $\frac{d}{l} = 0.25$ and $\frac{d}{l} = 0$ cross section, it is clear that the area of the initial negative region is high in $\frac{d}{l} = 0$ which effectively transfers large amount of energy from the body to the fluid and therefore resulting a low power output.

6.4.2 Surface pressure

In order to investigate further the cause of this negative region, surface pressure data of static DNS simulations were analysed of the isosceles triangle ($\frac{d}{l} = 0$) at $\theta = 4^\circ$, $\theta = 16^\circ$ and $\theta = 21^\circ$. These points lie in regions where the negative portion increases, the negative portion decreases and where C_y becomes positive respectively.

Figure 6.4 shows the surface pressure of the top and bottom surfaces of the body ($\frac{d}{l} = 0$) starting from the leading edges. At $\theta = 4^\circ$ The pressure of the bottom of the body is greater than the top. Therefore, a pressure difference is created and a force is generated in the upward direction which according to the sign convention presented in 2.1, against the velocity of the body, hence giving a negative C_y . As θ (figure 6.4 (b)) is increased, at 16° the gap between the surface pressure at the leading edge between the top and the bottom reduces. This effect results the increase in C_y (although it is still in the negative region). As θ is further increased at 21° (figure 6.4 (c)) the surface pressure on the top side becomes greater than the bottom. Therefore, the net effect of the pressure difference is a positive C_y which the driving force F_y is in phase with the velocity of the body.

6.4.3 Velocity profiles at the points of flow separation

Having established that the cause of the initial negative region of the C_y vs. θ plot was the pressure difference mainly at the leading edge of the top and bottom surfaces of the cross section, it was then further investigated the cause of this particular pressure difference.

A key variable which directly relates to the pressure fluid in motion is the velocity

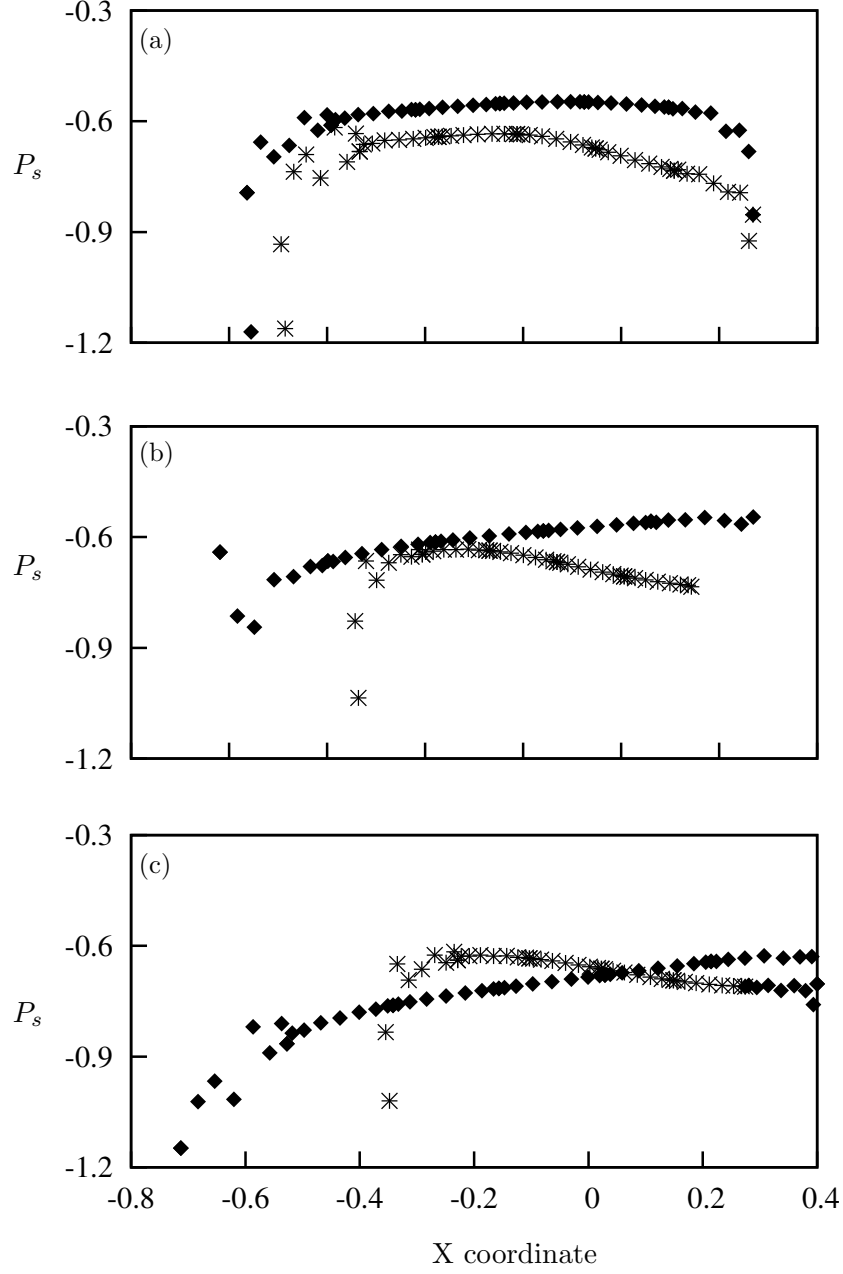


Figure 6.4: Surface pressure of top (\times) and bottom (\blacklozenge) surfaces of the static triangular cross section at (a) $\theta = 4^\circ$, (b) $\theta = 16^\circ$ and (c) $\theta = 21^\circ$. A clear pressure difference is visible between the surfaces. The top surface comparatively has more negative pressure where a lift is created which results in a negative C_y at 4° and reduces as θ is increased, while the vice versa occurs at the top surface.

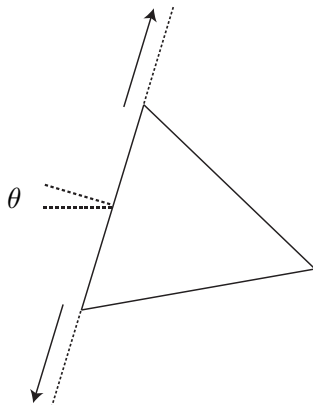


Figure 6.5: Illustration of the lines along which the flow velocity magnitudes have been extracted. The data have been extracted along a line starting from the separation points in the outward direction (shown with arrows) for the top and bottom surfaces.

of the fluid. The fundamentals of fluid dynamics state that pressure and velocity have an inversely proportional relationship in a Newtonian fluid. This is also evident in the Bernoulli's equation. Hence, analysis of the velocity at the edges of flow separation was performed to obtain a clear understanding about the cause of the pressure differences occurred.

In order to obtain a clear picture of the behaviour of the velocity, velocity magnitude data were obtained along lines spreading outwards starting from the top and bottom edges of flow separation. A clear illustration of these lines are depicted in figure 6.5. The lengths of these lines were equal to unity (equal to the frontal projected height of the body). Data were obtained for the same cases which the surface pressure data were obtained i.e. isosceles triangle ($\frac{d}{l} = 0$) at $\theta = 4^\circ$, $\theta = 16^\circ$ and $\theta = 21^\circ$.

The velocity profiles at the chosen three incident angles are presented in 6.6. A sudden rise of velocity magnitude could be observed at the flow separation points. The velocity magnitude at the top separation point at $\theta = 4^\circ$ (figure 6.6 (a)) is less than the bottom separation point, leading to a lower pressure at the top edge. However, the velocity magnitude at the bottom edge becomes greater than the top edge at $\theta = 16^\circ$. The difference between the velocity magnitude tends to broaden as θ is increased to 21° , while the velocity magnitude at the bottom being greater than the top (figure 6.6 (c)). This effectively creates

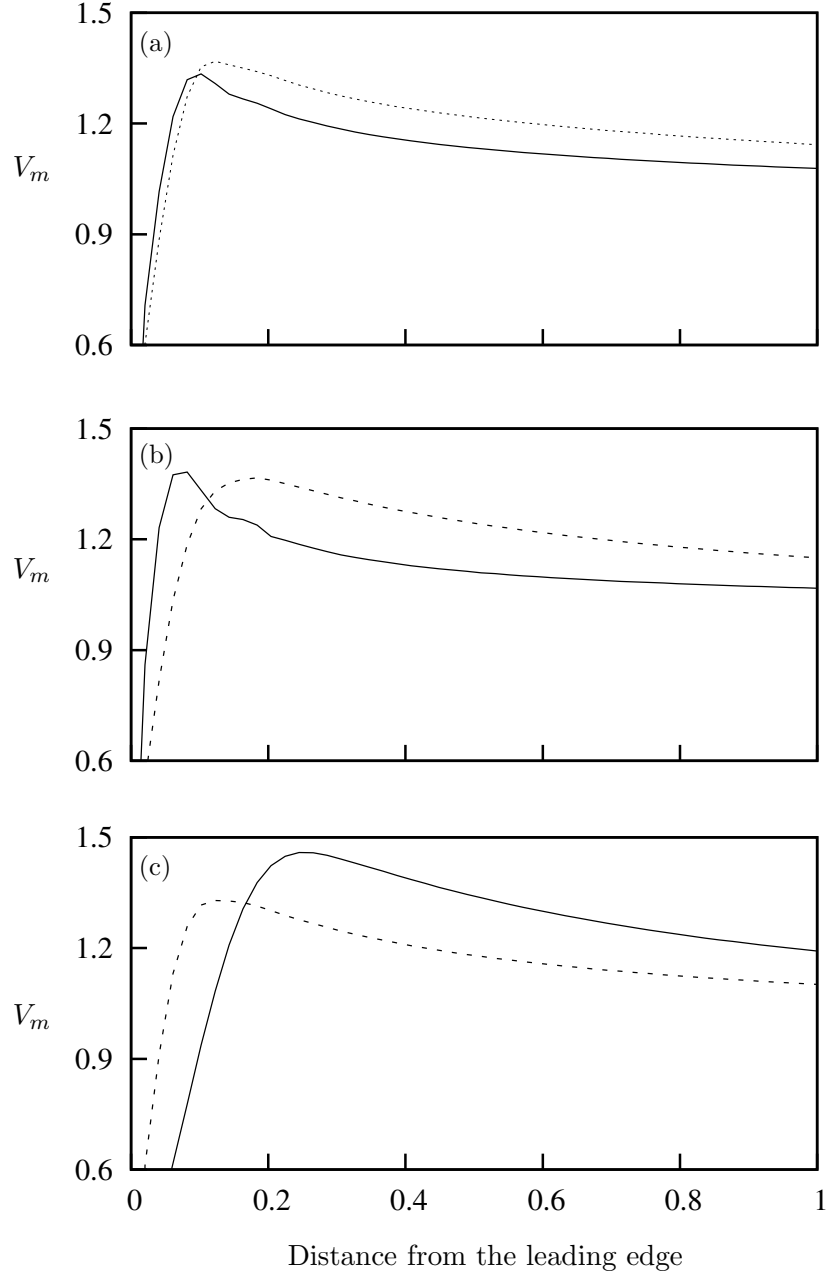


Figure 6.6: Velocity magnitudes of the flow along a line parallel to the front surface spreading towards top (---) and bottom (—) boundaries (figure 6.5). These two lines (for the top and bottom surfaces) start from the top and bottom leading edges of the triangular cross section. Data present (a) $\alpha = 4^\circ$, (b) $\alpha = 16^\circ$ and (c) $\alpha = 21^\circ$.

the pressure difference created in figure 6.4 (c), which leads to a positive C_y and results in a forcing which is in phase with the velocity of the body.

6.5 Fluid-structure interaction (DNS) results

6.5.1 Mean power data

As discussed in section 4.3.5 the main drawback of the QSS model is assuming that the only driving force of the system is F_y , which is generated from induced velocity. However, it was proved that this is not the case as vortex shedding have a significant influence with other non-linear disturbances on mean power as Π_1 decreases. Nevertheless, it was also concluded that a good agreement for power could be made at high Π_1 for the square cross section. Therefore, a comparison study between QSS and DNS mean power was carried out on the different cross section at high Π_1 ($= 1000$). As it was evident from figure 6.3 that the maximum power at $\frac{d}{l} = 0 < \frac{d}{l} = 0.25$, DNS mean power data were obtained between $0.25 \leq \frac{d}{l} \leq 1$. It should be noted that such steps had to be taken due to the prolong computational time taken to carry out the Direct numerical simulations.

Both DNS and QSS mean power data figure 6.7 show that $\frac{d}{l}$ decreases maximum mean extracted power increases following a similar trend. Thus these results reinforce the hypothesis for this section which is obtaining higher mean power by delaying the flow re-attachment.

However, a significant error (calculated using equation 4.9) between QSS and DNS power could be observed as $\frac{d}{l}$ increased. The quantified errors presented in 6.8 clearly shows the exponential increase in the % error as $\frac{d}{l} \rightarrow 0.25$. The likely cause of this significant error could be due to the non-linear interactions and the presence of non-linear forcing other than the induced force F_y .

6.5.2 Flow-filed data

In order to investigate further on the error between QSS and DNS results, flow-filed data were analysed on a selected cross section. The cross section selected to perform this task was $\frac{d}{l} = 0.25$ at $\Pi_2 = 0.26$ which is the case where the maximum mean power could be obtained in DNS data.

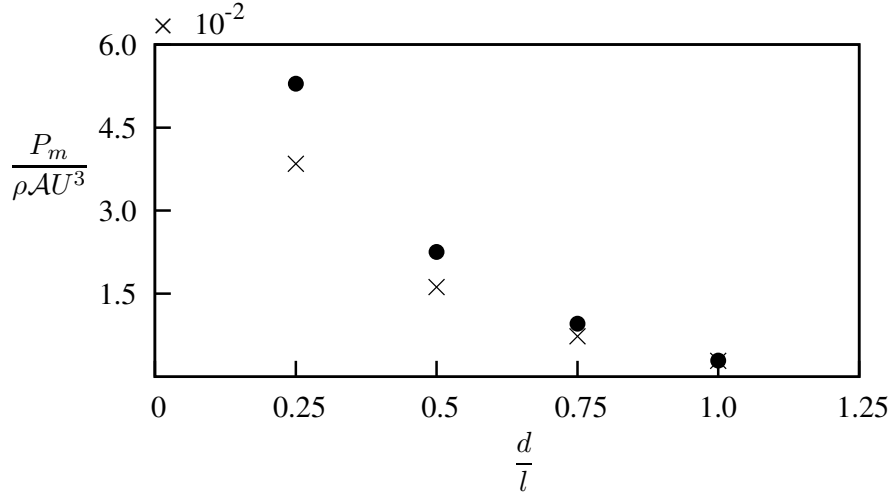


Figure 6.7: Comparison of the maximum power obtained using DNS (\bullet) data and predicted by QSS (\times) model as a function of $\frac{d}{l}$. Data obtained at $\Pi_1 = 1000$ ($m^* = 201.3$) and $Re = 200$. Similar trends are present for both QSS and DNS data. A significant reduction in power could be observed as $\frac{d}{l} \rightarrow 1$

The time averaged flow-fields were obtained at 3 selected points of the velocity signal. These points were point 1 where \dot{y} is maximum, point 2 where \dot{y} close to zero and further decreasing and point 3 where \dot{y} is close to zero but moving towards the positive direction. A depiction of these points are presented in 6.9. The averaging was carried out over a vortex-shedding cycle, where the starting and end times were defined to evenly bracket the point in consideration to attain the average flow-field at that point. Time averaged stationary flow-field data of the corresponding induced angles were also obtained for comparison.

Figure 6.10 shows the time averaged stream functions for points 1,2 and 3 and the stationary time averaged flow-field data for the corresponding induced angles. Comparison between FSI and stationary data at point 1 (Figure 6.10 (a) and (b)) shows a significant difference of the stream functions even at the leading edge.

In contrast, at point 2 and 3 the stream functions at the leading edge of the FSI simulations are similar to that of the stationary simulations. At point 2 both the FSI (figure 6.10 (b)) and stationary (figure 6.10 (c)) show similar flow behaviour until separation. A single circulation bubble at the top is formed in the FSI case where a symmetrical formation

6. INFLUENCE OF FLUID DYNAMICS OF THE SYSTEM ON THE EXTRACTED POWER

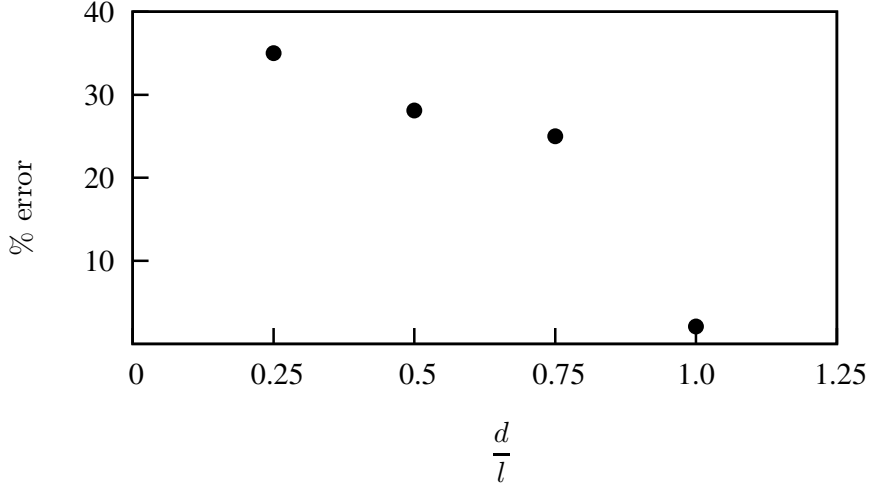


Figure 6.8: The percentage error between the maximum power obtained using DNS data and predicted by QSS model as a function of $\frac{d}{l}$. The error reduces significantly as $\frac{d}{l} \rightarrow 1$

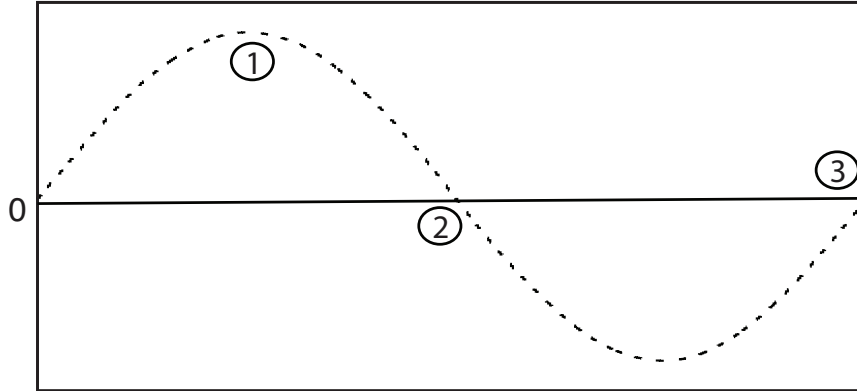


Figure 6.9: Illustration of the time history of velocity depicting the points considered to obtained time averaged flow-field data. The points considered are: the point where the velocity is at its maximum; where the velocity is zero and continues to decrease; where the velocity is zero and continues to increase.

of circulation bubbles could be observed in the stationary case. A similar behaviour of the stream functions could be observed between point 3 for FSI (figure 6.10 (d)) and stationary (figure 6.10 (e)) cases.

According to the assumptions of the QSS theory the flow-fields between the stationary and FSI cases at points 2 and 3 should be more or less identical as the induced velocities

are zero therefore the induced angles are zero. However, the observations of the FSI case is significantly different. This indicates that there are significant non linear forcing is present as $\frac{d}{l}$ decreases which could be a result of the higher induced angles and therefore the higher velocities involved.

Thus, one of the key conclusions could be gained is that the QSS predictions deviates significantly for mean power predictions as $\frac{d}{l}$ decreases. This is due to the fact that the forcing driving the system is not solely based on the induced velocity. Be that as it may the QSS model provides a reasonable predictions for power to obtain trends similar to DNS results. Therefore, QSS model could be used as a design and research tool to obtain preliminary data and conclusions to produce efficient galloping energy extraction systems.

6.5.3 Design considerations for a galloping energy extraction system through control of the fluid dynamics.

It is clear that delaying reattachment of the flow would lead to higher energy output. However, it is to be noted that even though a higher power output could be obtained by delaying separation, a region where the power is transferred from the body to the fluid will develop as $\frac{d}{l}$ is decreased. This can be observed through the negative region present in the C_y curves beyond $\frac{d}{l} < 0.25$. As this negative region develops the maximum power which could be extracted reduces. This was observed in the power curves (figure 6.4.1) where the maximum power of $\frac{d}{l} = 0$ was less than $\frac{d}{l} = 0.25$.

This fact leads to one important design consideration where the optimum cross section lies at the point where a balance of negative and positive regions could be obtained in the C_y vs. θ curve. Barrero-Gil et al. (2010) concluded that the first coefficient a_1 should satisfy $a_1 > 0$ in order to obtain for good operation of an energy harvesting system. Here, it is explained more in detailed using the QSS model together with direct numerical simulations of FSI cases.

As further consideration for future research, FSI and QSS work at $0 < \frac{d}{l} < 0.25$ could be carried out to find the optimum ratio of $\frac{d}{l}$ to obtain a maximum power output. Moreover, further work could be carried out investigate on the techniques to reduce the negative portion of the C_y curve by applying modifications to the cross section. One such example could be rounding the corners of the cross section.

6.6 Summary of Influence of fluid dynamics of the system on the extracted power

The primary objective of the work presented in this chapter was to test the hypothesis whether higher power output could be obtained by delaying the flow reattachment. This was done by incrementally tapering off the top and bottom sides of the square cross section. A negative region in the C_y vs. θ curve could be observed beyond $\frac{d}{l} < 0.25$. This region resulted in a power loss in a certain portion of the cycle as the driving force F_y and the velocity \dot{y} was out of phase.

The mean power vs. Π_2 curves showed an increase in maximum power as $\frac{d}{l}$ was decreased until $\frac{d}{l} = 0.25$. At $\frac{d}{l} = 0$ the maximum power was less than $\frac{d}{l} = 0.25$. Further analysis of the C_y curve revealed that the negative region of $\frac{d}{l} = 0$ is grater than $\frac{d}{l} = 0.25$ hence, resulting in a lower maximum power output.

Further investigations were carried out to find reasons for this negative region to exist. The surface pressure plots and the velocity magnitude profiles at the separation points revealed that this is due to the incidence angle and the cross section which resulted in changes in flow velocities at the separation points.

Comparison with between the QSS maximum power data and the FSI data showed similar trends where the maximum power increased when $\frac{d}{l}$ was decreased proving that the hypothesis was correct. Be that as it may the error between the QSS and FSI simulation increased drastically as $\frac{d}{l}$ was reduced. Further investigations carried out using time averaged flow-filed data concluded that the mean flow of FSI simulations had significant deviations with the DNS stationary simulations carried out at corresponding induced angles. This was a result of the body moving towards higher induced angles and thereby moving towards higher velocities as $\frac{d}{l}$ was decreased. Therefore the primary assumption of QSS which is considering F_y as the driving force of the system was no longer valid as other significant non-linear forcing was present in the system. Yet, the QSS model could be used as a tool to obtain initial approximations to design galloping energy harvesting systems as QSS data produced similar trends as the FSI simulations.

In order to obtain an efficient galloping one key design consideration is to obtain a cross section which has the optimum balance of the negative and positive regions of the C_y

vs. θ curve. Delaying the reattachment leads to higher power however as a consequence a negative region of C_y emerges in C_y curve and therefore, transferring power from the body to the fluid. This region keeps on increasing between $0 \leq \frac{d}{l} \leq 0.25$. Thus as a result an optimum $\frac{d}{l}$ should be obtained in order to get a balance between the negative and positive regions which leads to an efficient galloping energy harvesting system.

As for future research and development, a further design consideration could be investigating the possibility of reducing the negative region of the C_y curve by making alterations to the cross section such as rounding the edges of flow separation.

6. INFLUENCE OF FLUID DYNAMICS OF THE SYSTEM ON THE EXTRACTED POWER

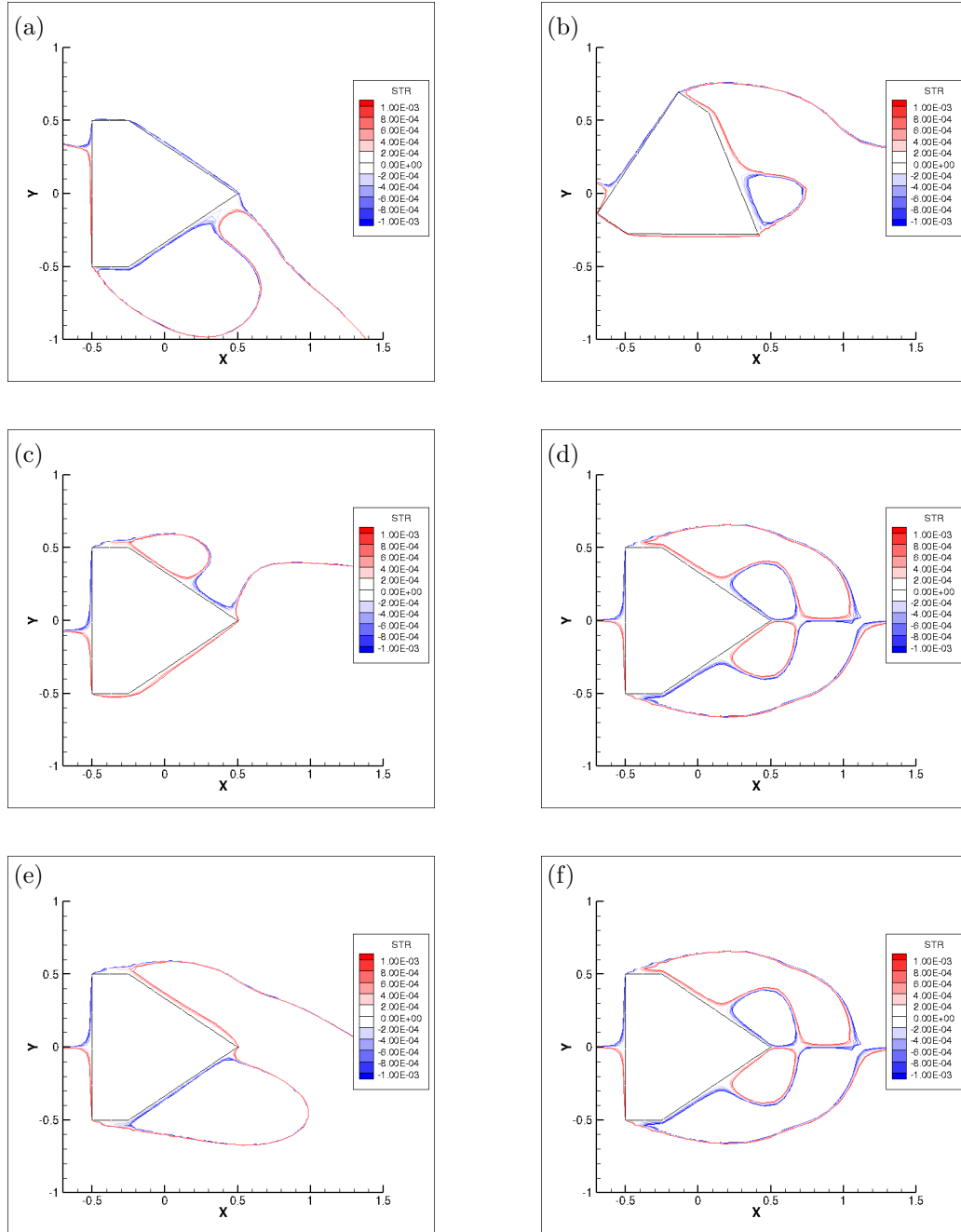


Figure 6.10: Time averaged stream functions of stationary and oscillating flow-fields of the hybrid cross section ($\frac{d}{T} = 0.25$), averaged over a vortex shedding cycle. (a), (c) and (e) the averaged stream functions of the oscillating case at $t = 2295.763$ (point 1), $t = 2305.897$ (point 2) and $t = 2325.870$ (point 3). (b), (d) and (f) are the stream functions of the flow field of the stationary body corresponding to the induced angles of (a), (c) and (e).

CHAPTER 7

CONCLUSIONS

A fundamental study was carried out to explore the potential of obtaining useful energy from fluid-elastic galloping. This research was based on numerical models and simulations. The study was primarily focused on understanding the energy transfer between the fluid and the structure.

As previously mentioned, since galloping was a fluid-structure mechanism two major objectives were identified for research namely, Understanding the underpinning structural parameters of the system and methods to optimise it for a better power output and understanding the fluid mechanics of the system and thereby obtain an optimum mean power output by controlling these mechanics. A third sub-objective was identified during the study of the first objective, which was to carry out a brief study of the frequency response to compliment the first objective of this research.

New governing dimensionless groups for galloping namely, Π_1 and Π_2 were formulated using the natural times-scales of the linearised quasi-steady state model. Data were obtained using a square cross section. The formulated dimensionless groups provided a good collapse for the predicted power output in comparison with the classical VIV parameters which have been traditionally used i.e. U^* and ζ . The collapsed dimensionless groups reinforces the argument the velocity amplitude to the system and the power transfer of the system does not depend on the natural frequency of the system over a large range of natural frequencies. Although equation 4.8 shows that m^* is an independent parameter, the data show that the system is essentially a function of Π_1 and Π_2 . A close inspection of

7. CONCLUSIONS

equation 4.8 reveals that m^* only has an impact on the non-linear forcing terms in relation to the velocity of the body. Thus in order for these non-linear terms to be acceptable, the induced angle of attack and therefore, the velocity of the body needs to be very large, which appears not to be the case for the range of parameters which were tested.

It could be concluded through comparison between the quasi-steady state and direct numerical simulation data, that the quasi-steady state model provides a good approximation of the power output of the system when Π_1 is relatively high. However, the QSS approximation is too close at low values of Π_1 due to the fact that QSS model does not account for the impact of vortex shedding which is shown to increase in influence as Π_1 is decreased. Be that as it may, the QSS model does provide a reasonable prediction of the value of Π_2 at which maximum power is produced. Both the error in predicted maximum power between the QSS and the DNS models and the relative power of the vortex shedding have been quantified and scale similar to $1/\sqrt{\Pi_1}$

A brief frequency study was carried out in order to complement the understanding of Π_1 and Π_2 . Using the eigenvalues of the system an expression for galloping frequency was formulated in terms of Π_1 and Π_2 . This frequency was defined as the linear frequency f_{lin} of the system. Based on this frequency two regions of frequency response were identified which were the linear frequency range where $f_{lin} > 0$ and the non-linear range where $f_{lin} = 0$. Both frequency data obtained using QSS model and DNS agreed well with f_{lin} within the boundaries of the DNS simulations where lower boundary of Π_1 was limited to $\Pi_1 = 10$ due to the weakening of the galloping signal.

The QSS frequency data tend to deviate from the linear frequency beyond $\Pi_1 < 10$. Implying the start of the influence of the non-linear forcing.

The QSS model kept providing a signal and hence a frequency in the non-linear frequency region. Thus, the comparison parameter was the unstamped natural frequency as $f_{lin} = 0$ and f_{DNS} could not be obtained from the signal processing techniques used. The data showed an acceptable agreement between $0.06 \geq$ but deviated as Π_1 reduced.

The mere existence of this non-linear frequency region was a question as no DNS data could be obtained, because the galloping signal was weak and the techniques used to obtain the frequency were not sensitive enough to capture these weak signals. Thus it was concluded that further investigations should be carried out on this region but was not pursued in this

study due to deviation of the major objective and scope and time constraints.

Yet, The linear expression of the galloping frequency formulated using Π_1 and Π_2 provided a excellent prediction within the boundaries where DNS data were obtained. This complimented the overall understanding and of the new formulated parameters Π_1 and Π_2 , completing the first objective of and the first phase of this research, *“Understanding the governing mechanical parameters of the system and isolate regions where a good power transfer could be obtained.”*

The second phase or the objective of this study was focused on optimisation of the governing fluid mechanics of the system in order to obtain a higher power output. The primary hypothesis was that delaying the flow re-attachment would lead to a higher power output. The square cross section was systematically tapered off by changing the $\frac{d}{l}$ ratio in order to achieve this.

One interesting observation was the presence of a negative region of the C_y vs. θ curve beyond $\frac{d}{l} \leq 0$. Thus, a loss of power could be observed in a certain portion of the galloping cycle was present as due to the fact that the velocity and the transverse forcing F_y was out of phase.

It was observed that the maximum mean power increases as $\frac{d}{l}$ was decreased until $\frac{d}{l} = 0.25$. However, further analysis revealed that the maximum power at $\frac{d}{l} = 0.25$ was grater than $\frac{d}{l} = 0$ which was a direct result of the size of the negative region of the C_y vs. θ curve. Thus it could be concluded that the initial hypothesis could be proven but with some conditions.

Further investigation of the surface pressure data and the velocity magnitude data revealed that the changes in flow velocities at the separation points, as a result of the shape of the cross section and the incidence angle caused this negative region of the C_y plot.

Comparison of QSS maximum power data and FSI data provided similar trends of maximum power being increased as $\frac{d}{l}$ was increased proving the initial hypothesis. However, the error between the QSS and FSI maximum power data increased exponentially as $\frac{d}{l}$ reduced. Investigations carried out using time averaged flow-filed data concluded that the mean flow of the FSI simulations had a significant deviation with the corresponding stationary DNS data. This was a result of the incurred higher traverse velocities as $\frac{d}{l}$ was decreased. AS a result significant non-linear forcing was present resulting a deviation from

the quasi-steady hypothesis. Be that as it may, as concluded is phase one of this study QSS model could be used as a tool to obtain initial qualitative approximations to design galloping energy harvesting systems.

It could be concluded that a key design consideration in obtaining a optimum cross section for energy harvesting is to find a good balance between the negative and positive regions of the C_y vs. θ curve. Delaying reattachment is beneficial however, the presence of the negative region of the C_y curve will have a adverse effect on power transfer.

Future research and development was also discussed in this phase. A further design considerations could be considered, for example, investigating the possibility of reducing the negative region of the C_y curve by making alterations to the cross section such as rounding the edges of flow separation.

Therefore, the second phase was concluded and the second objective of this study was achieved which was: *“Understand the governing fluid mechanics of the system and to optimise and control these mechanics in order to obtain a higher power transfer.”*

BIBLIOGRAPHY

- Alonso, G., Meseguer, J., Pérez-Grande, I., 2005. Galloping instabilities of two-dimensional triangular cross-section bodies. *Experiments in Fluids* 38, 789–795.
- Alonso, G., Meseguer, J., Sanz-Andrés, A., Valero, E., 2010. On the galloping instability of two-dimensional bodies having elliptical cross-sections. *Journal of Wind Engineering and Industrial Aerodynamics* 38, 789–795.
- Alonso, G., Valero, E., Meseguer, J., 2009. An analysis on the dependence on cross section geometry of galloping stability of two-dimensional bodies having either biconvex or rhomboidal cross sections. *European Journal of Mechanics B/Fluids* 28, 328–334.
- Barrero-Gil, A., Alonso, G., Sanz-Andres, A., Jul. 2010. Energy harvesting from transverse galloping. *Journal of Sound and Vibration* 329 (14), 2873–2883.
- Barrero-Gil, A., Sanz-Andrés, A., Roura, M., Oct. 2009. Transverse galloping at low Reynolds numbers. *Journal of Fluids and Structures* 25 (7), 1236–1242.
- Bearman, P. W., Gartshore, I. S., Maull, D. J., Parkinson, G. V., 1987. Experiments on flow-induced vibration of a square-section cylinder. *Journal of Fluids and Structures* 1, 19–34.
- Bernitsas, M. M., Ben-Simon, Y., Raghavan, K., Garcia, E. M. H., 2009. The VIVACE Converter: Model Tests at High Damping and Reynolds Number Around 10^5 . *Journal of Offshore Mechanics and Arctic Engineering* 131 (1), 011102.
- Bernitsas, M. M., Raghavan, K., Ben-Simon, Y., Garcia, E. M. H., 2008. VIVACE (Vortex Induced Vibration Aquatic Clean Energy): A new concept in generation of clean and

BIBLIOGRAPHY

- renewable energy from fluid flow. *Journal of Offshore Mechanics and Arctic Engineering* 130 (4), 041101–15.
- Blevins, R. D., 1990. *Flow-Induced Vibration*, 2nd Edition. New York: Van Nostrand Reinhold.
- Bouclin, D. N., 1977. Hydroelastic oscillations of square cylinders. Master's thesis, University of British Columbia.
- Den Hartog, J. P., 1956. *Mechanical Vibrations*. Dover Books on Engineering. Dover Publications.
- Deniz, S. and Staubli, T., 1997. Oscillating rectangular and octagonal profiles: Interaction of leading-and trailing-edge vortex formation. *Journal of Fluids and Structures* 11, 3–31.
- Fletcher, C. A. J., 1984. *Computational Galerkin methods*. Springer-Verlag, New York.
- Fletcher, C. A. J., 1991. *Computational techniques for fluid dynamics*. Vol. 1. Springer-Verlag, New York. Gabbai,.
- Glauert, H., 1919. The rotation of an aerofoil about a fixed axis. Tech. rep., Advisory Committee on Aeronautics R and M 595. HMSO, London.
- Griffith, M. D., Leontini, J. S., Thompson, M. C., Hourigan, K., 2011. Vortex shedding and three-dimensional behaviour of flow past a cylinder confined in a channel. *Journal of Fluids and Structures* 27 (5-6), 855–860.
- Joly, A., Etienne, S., Pelletier, D., Jan. 2012. Galloping of square cylinders in cross-flow at low Reynolds numbers. *Journal of Fluids and Structures* 28, 232–243.
- Karniadakis, G. E., Sherwin, S., 2005. *Spectral/hp element methods for computational fluid dynamics*, ii Edition. Oxford University.
- Kreyszig, E., 2010. *Advanced Engineering Mathematics*, 10th Edition. John Wiley & Sons.
- Lee, J., Bernitsas, M., Nov. 2011. High-damping, high-Reynolds VIV tests for energy harnessing using the VIVACE converter. *Ocean Engineering* 38 (16), 1697–1712.

- Lee, J., Xiros, N., Bernitsas, M., Apr. 2011. Virtual damperspring system for VIV experiments and hydrokinetic energy conversion. *Ocean Engineering* 38 (5-6), 732–747.
- Leontini, J. S., 2007. A numerical investigation of transversely-oscillating cylinders in two-dimensional flow. Ph.D. thesis, Monash University.
- Leontini, J. S., Lo Jacono, D., Thompson, M. C., Nov. 2011. A numerical study of an inline oscillating cylinder in a free stream. *Journal of Fluid Mechanics* 688, 551–568.
- Leontini, J. S., Thompson, M. C., 2013. Vortex-induced vibrations of a diamond cross-section: Sensitivity to corner sharpness. *Journal of Fluids and Structures* 39, 371–390.
- Leontini, J. S., Thompson, M. C., Hourigan, K., Apr. 2007. Three-dimensional transition in the wake of a transversely oscillating cylinder. *Journal of Fluid Mechanics* 577, 79.
- Luo, S., Chew, Y., Ng, Y., Aug. 2003. Hysteresis phenomenon in the galloping oscillation of a square cylinder. *Journal of Fluids and Structures* 18 (1), 103–118.
- Luo, S. C., Yazdani, M., Chew, Y. T., Lee, T. S., 1994. Effects of incidence and afterbody shape on flow past bluff cylinders. *Journal of Wind Engineering* 53, 375–399.
- Nakamura, Y., Mizota, T., 1975. Unsteady lifts and wakes of oscillating rectangular prisms. *ASCE Journal of the Engineering Mechanics Division* 101, 855–871.
- Nakamura, Y., Tomonari, Y., 1977. Galloping of rectangular prisms in a smooth and in a turbulent flow. *Journal of Sound and Vibration* 52, 233–241.
- Naudascher, E., Rockwell, D., 1994. *Flow-induced vibrations: An engineering guide*. A.A. Balkema, Rotterdam.
- Naudascher, E., Wang, Y., 1993. Flow induced vibrations of prismatic bodies and grids of prisms. *Journal of fluids and structures* 7, 341–373.
- Ng, Y., Luo, S., Chew, Y., Jan. 2005. On using high-order polynomial curve fits in the quasi-steady theory for square-cylinder galloping. *Journal of Fluids and Structures* 20 (1), 141–146.
- Païdoussis, M., Price, S., de Langre, E., 2010. *Fluid-Structure Interactions : Cross-Flow-Induced Instabilities*. Cambridge University Press.

BIBLIOGRAPHY

- Parkinson, G., 1989. Phenomena and modelling of flow-induced vibrations of bluff bodies. *Progress in Aerospace Sciences* 26, 169–224.
- Parkinson, G., Brooks, N. P. H., 1961. On the aeroelastic instability of bluff cylinders. *Journal of Applied Mechanics* 28, 252–258.
- Parkinson, G. V., 1974. Mathematical models of flow-induced vibrations of bluff bodies. In *Flow-Induced Structural Vibrations*, e. naudascher Edition. Berlin: SpringerVerlag.
- Parkinson, G. V., Smith, J. D., 1964. The square prism as an aeroelastic non-linear oscillator. *The Quarterly Journal of Mechanics and Applied Mathematics* 17 (2), 225–239.
- Pregalato, C., 2003. Flow-induced vibrations of a tethered sphere. Ph.D. thesis, Monash University.
- Raghavan, K., Bernitsas, M., Apr. 2011. Experimental investigation of Reynolds number effect on vortex induced vibration of rigid circular cylinder on elastic supports. *Ocean Engineering* 38 (5-6), 719–731.
- Raghavan, K., Bernitsas, M. M., Maroulis, D. E., 2009. Effect of Bottom Boundary on VIV for Energy Harnessing at $8 \times 10^3 < Re < 1.5 \times 10^5$. *Journal of Offshore Mechanics and Arctic Engineering* 131 (3), 031102.
- Robertson, I., Li, L., Sherwin, S. J., Bearman, P. W., 2003. A numerical study of rotational and transverse galloping rectangular bodies. *Journal of Fluids and Structures* 17, 681 – 699.
- Ruscheweyh, H., Hortmanns, M., Schnakenberg, C., 1996. Vortex-excited vibrations and galloping of slender elements. *Journal of Wind Engineering and Industrial Aerodynamics* 65, 347–352.
- Sheard, G. J., Fitzgerald, M. J., Ryan, K., Jun. 2009. Cylinders with square cross-section: wake instabilities with incidence angle variation. *Journal of Fluid Mechanics* 630, 43.
- Thompson, M., Hourigan, K., Sheridan, J., Feb. 1996. Three-dimensional instabilities in the wake of a circular cylinder. *Experimental Thermal and Fluid Science* 12 (2), 190–196.

- Thompson, M. C., Hourigan, K., Cheung, A., Leweke, T., Nov. 2006. Hydrodynamics of a particle impact on a wall. *Applied Mathematical Modelling* 30 (11), 1356–1369.
- Tong, X., Luo, S., Khoo, B., Oct. 2008. Transition phenomena in the wake of an inclined square cylinder. *Journal of Fluids and Structures* 24 (7), 994–1005.
- Tu, J., Yeoh, G., Liu, C., 2008. *Computational Fluid Dynamics: A Practical Approach*, 1st Edition. Butterworth-Heinemann.
- Vicente-Ludlam, D., Barrero-Gil, A., Velazquez, A., 2014. Optimal electromagnetic energy extraction from transverse galloping. *Journal of Fluids and Structures* 51, 281–291.
- Vio, G., Dimitriadis, G., Cooper, J., Oct. 2007. Bifurcation analysis and limit cycle oscillation amplitude prediction methods applied to the aeroelastic galloping problem. *Journal of Fluids and Structures* 23 (7), 983–1011.
- Weaver, D. S., Veljkovic, I., 2005. Vortex shedding and galloping of open semi-circular and parabolic cylinders in cross-flow. *Journal of Fluids and Structures* 21, 65–74.
- White, F., 1999. *Fluid mechanics*, 4th Edition. McGraw-Hill, Boston.